Ore Geology Reviews 163 (2023) 105747

Contents lists available at ScienceDirect

Ore Geology Reviews

journal homepage: www.elsevier.com/locate/oregeorev

Garnet U-Pb dating and magnetite geochemistry: Constraints on the origin of Fe mineralization in the Huogeqi polymetallic deposit, Northern China

Chongwen Xu [a], Xu Zhao [a,b,*], Jan Marten Huizenga [c,d,e], Junhao Wei [a], Yue Hu [a,f], Zhixin Zhao [a]

[a] School of Earth Resources, China University of Geosciences, Wuhan 430074, China
[b] Guangzhou Institute of Geochemistry, Chinese Academy of Sciences, Guangzhou 510640, China
[c] Faculty of Environmental Sciences and Natural Resource Management, Norwegian University of Life Sciences, P.O. Box 5003, NO-1432 Ås, Norway
[d] Economic Geology Research Institute (EGRU), College of Science and Engineering, James Cook University, Townsville, QLD 4811, Australia
[e] Department of Geology, University of Johannesburg, P.O. Box 524, Auckland Park 2006, South Africa
[f] Shandong Gold Geological and Mineral Exploration Co., Ltd., Yantai 261499, China

ARTICLE INFO

Keywords:
Huogeqi polymetallic deposit
Garnet U-Pb dating
Langshan
Magnetite
Mineral geochemistry

ABSTRACT

The Huogeqi Fe polymetallic deposit, which contains 48.17 Mt Fe, occurs in tremolite-diopside rocks of the Neoproterozoic Langshan Group in the north China. This study focuses on the magnetite mineralogy, texture and chemical composition, and U-Pb geochronology of garnet associated with magnetite and zircon from the granitoid related to mineralization in order to constrain the origin of Fe mineralization in Huogeqi deposit. LA-ICP-MS U-Pb dating of magnetite-bearing garnets yields a lower intercept age of 277.5 ± 8.7 Ma, which is coeval with the emplacement age of the mineralized-related granitoid (275.3 ± 1.3 Ma). Three types of magnetite were formed in the Huogeqi deposit, including Mt-A (coarse-grained disseminated), Mt-B (stratiform and fine-grained dense disseminated), and Mt-C (massive). The Mt-A can be subdivided into high-Ti Mt-A1 and relatively low-Ti porous and fractured Mt-A2. The Mt-B can be subdivided into porous Mt-B1 with relatively high V and low Ti contents, dark porous Mt-B2 with a relatively low V contents, porous inclusion-rich Mt-B3 with low Fe and V contents, and high Si and Mg contents, and less-porous Mt-B4 with low Si and Mg contents. The Mt-C includes porous Mt-C1 with a low Ti contents and high Si, Al, Mn contents and less-porous Mt-C2 with low Si, Al, and Mn contents. The decreasing Ti and V contents in the subsequent magnetite types indicate progressive cooling of the mineralizing fluid, increasing oxygen fugacity, and more intense fluid-rock interaction. Dissolution and re-precipitation played an important role in the formation of different generations of magnetite of Mt-B and Mt-C. The magnetite from Huogeqi deposit has a high Ni/Cr mass ratio, a high Fe content, and a high (Ca + Al + Mn) value, and a low V content, a low Ni/(Cr + Mn) mass ratio, and a low (Ti + V) value. These geochemical characteristics indicate that the magnetite has a hydrothermal origin in a skarn-type deposit, which is related to Early Permian magmatism in the Langshan area in north China.

1. Introduction

The Langshan metallogenic belt (LSMB) is located in the western segment of the northern margin of the North China Craton. It is an important polymetallic metallogenic belt in northern China, which includes the Huogeqi Fe-Cu-Pb-Zn, Dongshengmiao Cu-Pb-Zn and Tanyaokou Cu-Pb-Zn polymetallic deposit (Fig. 1b). The polymetallic Huogeqi deposit comprise Cu, Pb, Zn, and Fe whereas the other deposits only contain Cu, Pb, and Zn. Other differences between the Huogeqi deposit and other deposits in the region are related to the mineralization age and geochemistry. The zircon U-Pb chronology and Hf isotopic compositions indicate that the Huogeqi deposit is associated with the Neoproterozoic rift system of the northern LSMB whereas the Dongshengmiao and Tanyaokou deposits are related to the Mesoproterozoic rift system of the southern LSMB (Wang et al., 2016; Bao et al., 2019). The Huogeqi deposit shows an extremely high radiogenic Pb composition whereas the other polymetallic deposits are characterized by non-radiogenic Pb isotopic composition and a Proterozoic Pb-Pb model age (Gao et al., 2019). Zhong et al., (2012), Zhong and Li (2016) proposed a *syn*-sedimentary origin for Huogeqi Fe deposit and an epigenetic

* Corresponding author at: School of Earth Resources, China University of Geosciences, Lumo Road No. 388, Hongshan District, Wuhan 430074, Hubei Province, China.
E-mail address: xuzhao19@cug.edu.cn (X. Zhao).

https://doi.org/10.1016/j.oregeorev.2023.105747
Received 25 May 2023; Received in revised form 17 October 2023; Accepted 24 October 2023
Available online 14 November 2023
0169-1368/© 2023 The Author(s). Published by Elsevier B.V. This is an open access article under the CC BY-NC-ND license (http://creativecommons.org/licenses/by-nc-nd/4.0/).

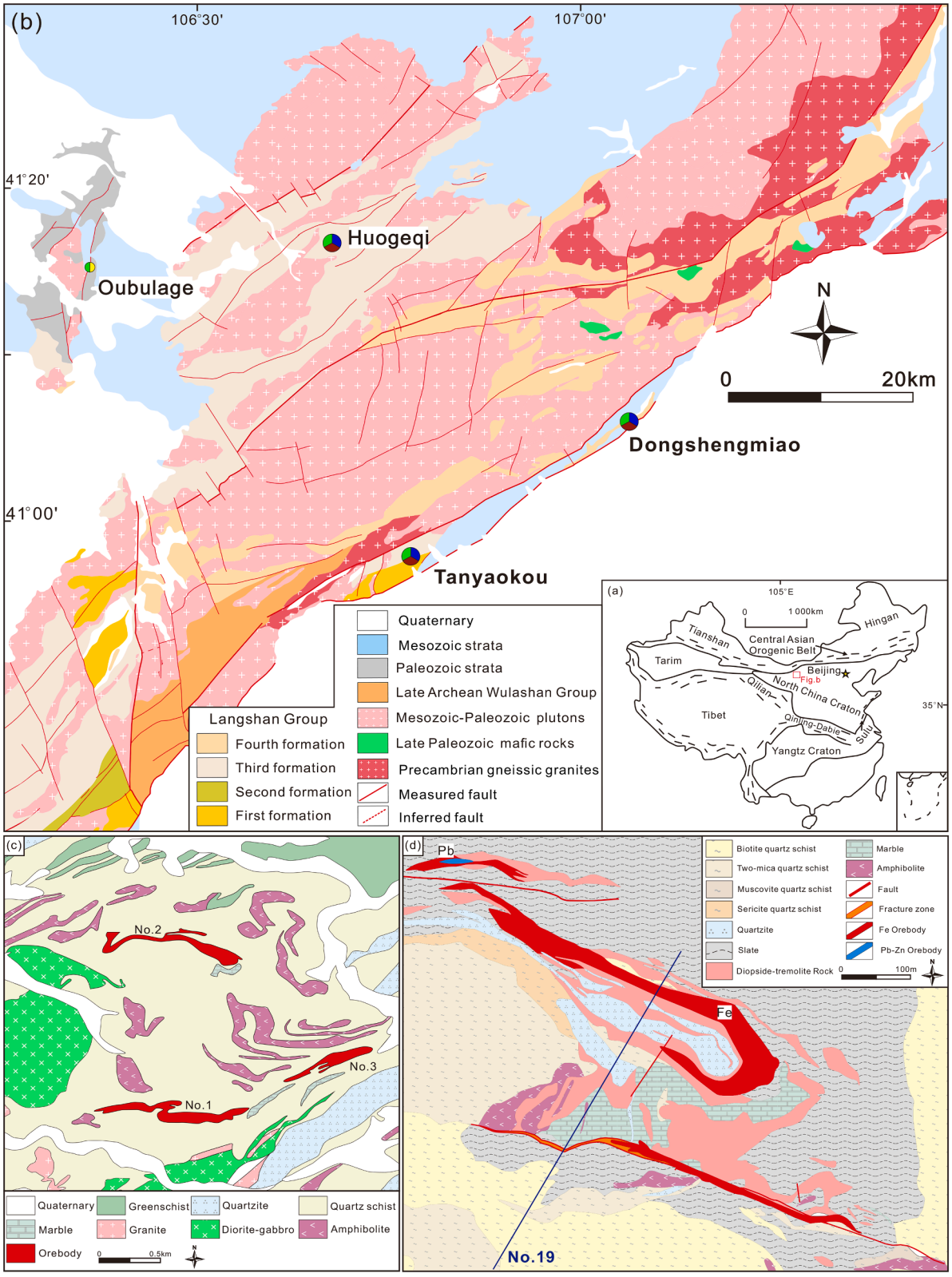

Fig. 1. (a) Simplified map of China; (b) Geological map (dashed red rectangle in Fig. 1a) of the Langshan metallogenic belt (LSMB), (c) Huogeqi polymetallic orefield, and (d) No. 2 Fe deposit. (For interpretation of the references to colour in this figure legend, the reader is referred to the web version of this article.)

metamorphic hydrothermal origin for the Cu-Pb-Zn ore bodies. Bao (2016) proposed that the Huogeqi polymetallic deposit is a typical magmatic-hydrothermal deposit. Gao et al. (2019) argued that the Huogeqi polymetallic deposit is a hydrothermal deposit related to the Indosinian magmatism and that the stratified deposit in the southern LSMB was part of the Proterozoic metallogenic system. It is still unknown, which factors resulted in the exclusive occurrence of Fe in the Huogeqi deposit.

Magnetite is the main Fe-bearing mineral in the Huogeqi Fe deposit, and can be used to provide insight on the mineralization types and

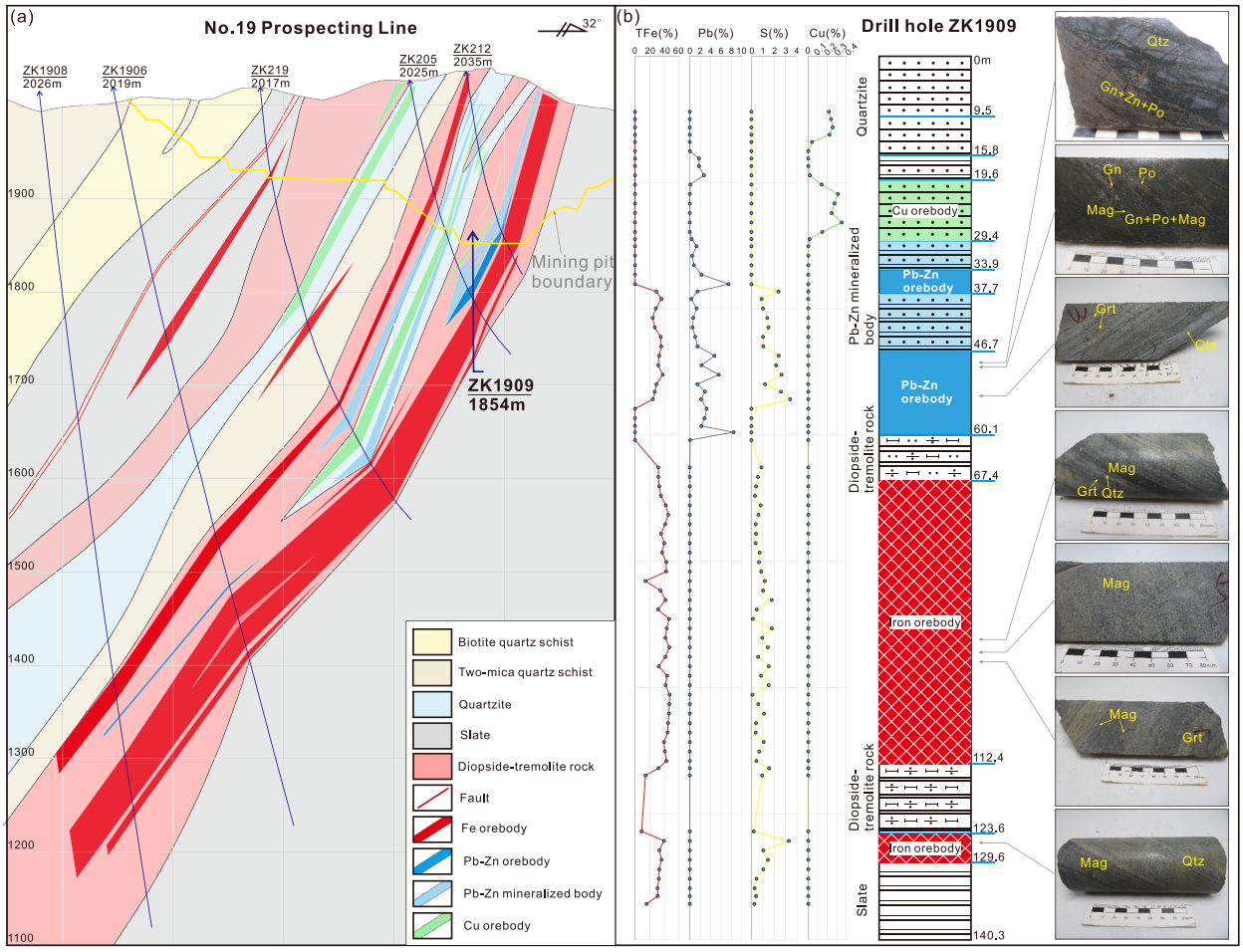

Fig. 2. (a) Geologic profile of No. 19 prospecting line in the Huogeqi No. 2 Fe deposit. (b) Schematic stratigraphic columns of drill core ZK1909. Abbreviations: Mag = magnetite; Sp = sphalerite; Gn = galena; Po = pyrrhotite; Grt = garnet; Qz = quartz.

genesis of iron deposits (Dupuis and Beaudoin, 2011; Dare et al., 2014; Zhao et al., 2022). Some trace elements (e.g., Al, Mn, Ti, V, Cr, Co, Sn, Ga and Mg) can be incorporated into the inverse spinel structure of magnetite by substituting Fe^{2+} and Fe^{3+} in the tetrahedral or octahedral sites (Dupuis and Beaudoin, 2011; Nadoll et al., 2014; Hu et al., 2015; Huang and Beaudoin, 2019). These elements have different partition coefficients for magnetite in a hydrothermal and magmatic system (Dupuis and Beaudoin, 2011; Nadoll et al., 2014; Huang and Beaudoin, 2019), i.e. the trace-element geochemical characteristics of magnetite can be used to determine whether magnetite has a hydrothermal or magmatic origin (Dare et al., 2014; Wen et al., 2017). The magnetite texture and composition can also be used to determine the physico-chemical conditions during ore-formation (Dupuis and Beaudoin, 2011; Dare et al., 2014; Wu et al., 2019).

In this study, we present the results of (1) mineralogical study of the different magnetite types of the Fe Huogeqi ore deposit, and (2) U-Pb age dating of garnet that is associated with the Fe mineralization. The objectives of this study are to determine the age of Fe mineralization and the origin of the different magnetite types with the aim to constrain the ore-forming processes.

2. Geological setting

2.1. Regional geology

The Langshan metallogenic belt (LSMB) is situated in the north China. The exposed strata in the area include the Late Archaean Wulashan Group, the Neoproterozoic Langshan Group, Paleozoic-Mesozoic sedimentary strata, and Quaternary sedimentary rocks (Fig. 1b). The Late Archaean Wulashan Group is the oldest metamorphic basement in the LSMB and comprises gneiss, granulite, amphibolite and marble (Liu et al., 2019a, Liu et al., 2019b). The overlying Neoproterozoic Langshan Group, is composed of mica-quartz-schist, andalusite-mica-schist, carbonaceous slate, marble, quartzite, diopside-tremolite rock, and amphibolite (Peng et al., 2005). The Neoproterozoic Langshan Group is unconformably overlain by the Paleozoic to Mesozoic sedimentary rocks that include shallow-marine clastic and carbonate sedimentary rocks of the Amushan Formation (Guo et al., 2019), and terrigenous clastic sedimentary rocks of the Dahongshan (Lin et al., 2022) and Lisangou Formations (Xin et al., 2000).

Precambrian granite gneisses occur mostly in the eastern part of the LSMB, and their exposure area is second only to that of Paleozoic-Mesozoic intrusive rocks (Fig. 1b). The Paleozoic-Mesozoic magmatic rocks in the Langshan area were formed during the Silurian (444–413 Ma), Carboniferous (346–299 Ma), Permian (293–251 Ma) and Triassic (245–230 Ma) (Wang et al., 2021). The Paleozoic-Mesozoic magmatic rocks include granite, granodiorite, and intermediate to mafic intrusive rocks (Zhong et al., 2013; Pi et al., 2015), and the petrogenesis and tectonic setting for these rocks generated in different periods could be summarized as follows: (1) The assemblages of Early Silurian calc-alkaline arc magma (Zhang et al., 2019), Carboniferous high Ba-Sr granite, and gabbro derived from enriched mantle source (Wang et al., 2015; Zheng et al., 2019; Zhang et al., 2020) indicate that the LSMB was mainly in a subduction setting during Early Silurian to Carboniferous. (2) The emplacement of Early–Middle Permian calc-alkaline I-type granitoid, A2-type granite, calc-alkaline mafic intrusive rocks (Zheng

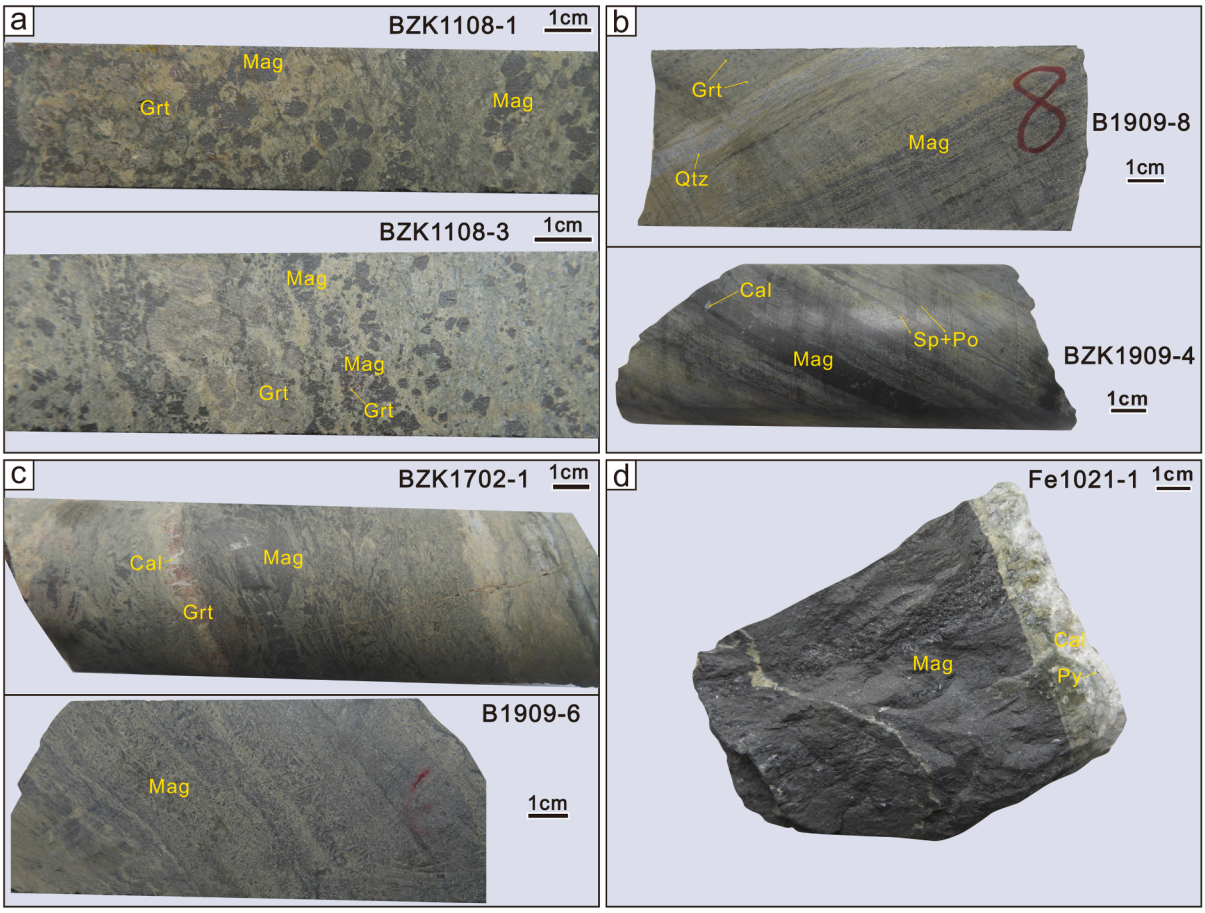

Fig. 3. Representative photographs of iron ore samples from Huogeqi Fe deposit. (a) Disseminated coarse self-shaped magnetite ore. (b) Stratiform magnetite-tremolite ore. (c) Fine-grained dense disseminated ore. (d) Massive magnetite ore. Abbreviations: Mag = magnetite; Py = pyrite; Grt = garnet; Cal = calcite.

et al., 2019), and the Qagan Qulu ophiolite (Zheng et al., 2014) implies that the LSMB was in a back-arc extensional setting, which is supported by the sedimentary sequence change from fluvial to shallow-marine environments during Early–Middle Permian (Guo et al., 2019). (3) The Middle–Late Permian adakitic granite sourced from partial melting of thickened continental lower crust (Hui et al., 2021), and Triassic high-K calc-alkaline to shoshonitic series granite derived from partial melting of the ancient crust are indicative of a collision setting (Wang et al., 2017; Wang et al., 2018). However, the timing of the final closure of the Paleo-Asian Ocean, are still under debate. Three views on the timings of the Ocean closure have been proposed by previous studies: (1) in the Late Devonian–Early Carboniferous (Xu et al., 2013; Chen et al., 2021; Wang et al., 2021), (2) in the Middle Permian (Zhang et al., 2009; Wang et al., 2020; Hui et al., 2021; Tian et al., 2021; Zheng et al., 2021), (3) late than the Middle Triassic (Zheng et al., 2021). Even if the debate remains, the widely distributed Permian granitoids, especially magmatic flare-up of ca. 280–ca. 270 Ma, represent the dominant tectonic-thermal event in the northern margin of the North China Craton (Gao et al., 2018).

The main regional structures include the Langshan anticlinorium, NE- and NS-trending regional faults, and the NE-, NW- and NS-trending secondary faults (Fig. 1b). The NE-trending regional faults control the distribution of sedimentary and magmatic rocks and the distribution of ore deposits, and the NW- and NS-trending secondary faults cut the NE-trending ore bodies.

Large and giant polymetallic deposits hosted by the Neoproterozoic Langshan Group occur in the Langshan area and include the Huogeqi Fe-Cu-Pb-Zn, the Dongshengmiao Cu-Pb-Zn, and the Tanyaokou Cu-Pb-Zn deposits (Fig. 1b). The Huogeqi Fe polymetallic deposit contains magnetite ore with an estimated Fe ore reserves of 48.17 Mt. The Langshan area contains Cu-Au deposits associated with Early-Middle Permian magmatism in the LSMB and adjacent areas including the Oubulage Cu-Au (264.3 ± 0.5 Ma, quartz ^{40}Ar-^{39}Ar age; Li et al., 2010a) and the Zhulazhaga Au deposit (282.3 ± 0.9 Ma, quartz ^{40}Ar-^{39}Ar age; Li et al., 2010b).

2.2. Deposit geology

The Huogeqi polymetallic orefield is located in the north of the LSMB and hosted in the Neoproterozoic Langshan Group. It has a Cu reserve of 0.71 Mt at an average grade of 1.35 % Cu, a Fe reserve of 48.17 Mt at an average grade of 34.68 % Fe, a Zn reserve of 0.99 Mt at an average grade of 1.34 % Zn, and a Pb reserve of 1.03 Mt at an average grade of 1.39 % Pb (Huang et al., 2001). The Huogeqi orefield includes No. 1 deposit to the south, No. 2 deposit to the north, and No. 3 deposit to the east (Fig. 1b, c). The No. 1 deposit is the largest deposit dominated by Cu, Pb, and Zn (Huang et al., 2001; Zhong et al., 2012). The No. 2 deposit is primarily a Fe deposit and accompanied by Cu and Pb-Zn orebodies. The No. 3 deposit is also a Fe deposit and of limited economic importance (Huang et al., 2001; Zhong et al., 2012). The Cu orebodies are hosted in quartzite, the Pb-Zn orebodies are hosted in carbonaceous slate, and the Fe orebodies are hosted in diopside-tremolite rock (Fig. 2). In addition to the ore-hosting lithologies, other exposed rocks include greenschist, quartz schist and marble of the Langshan Group, and Quaternary sedimentary rocks. The exposed magmatic rocks include Neoproterozoic amphibolite (Bao et al., 2019) and Permian diorite-gabbro and granite (Fig. 1c).

In the No. 2 Fe deposit, the exposed lithology includes quartz schist,

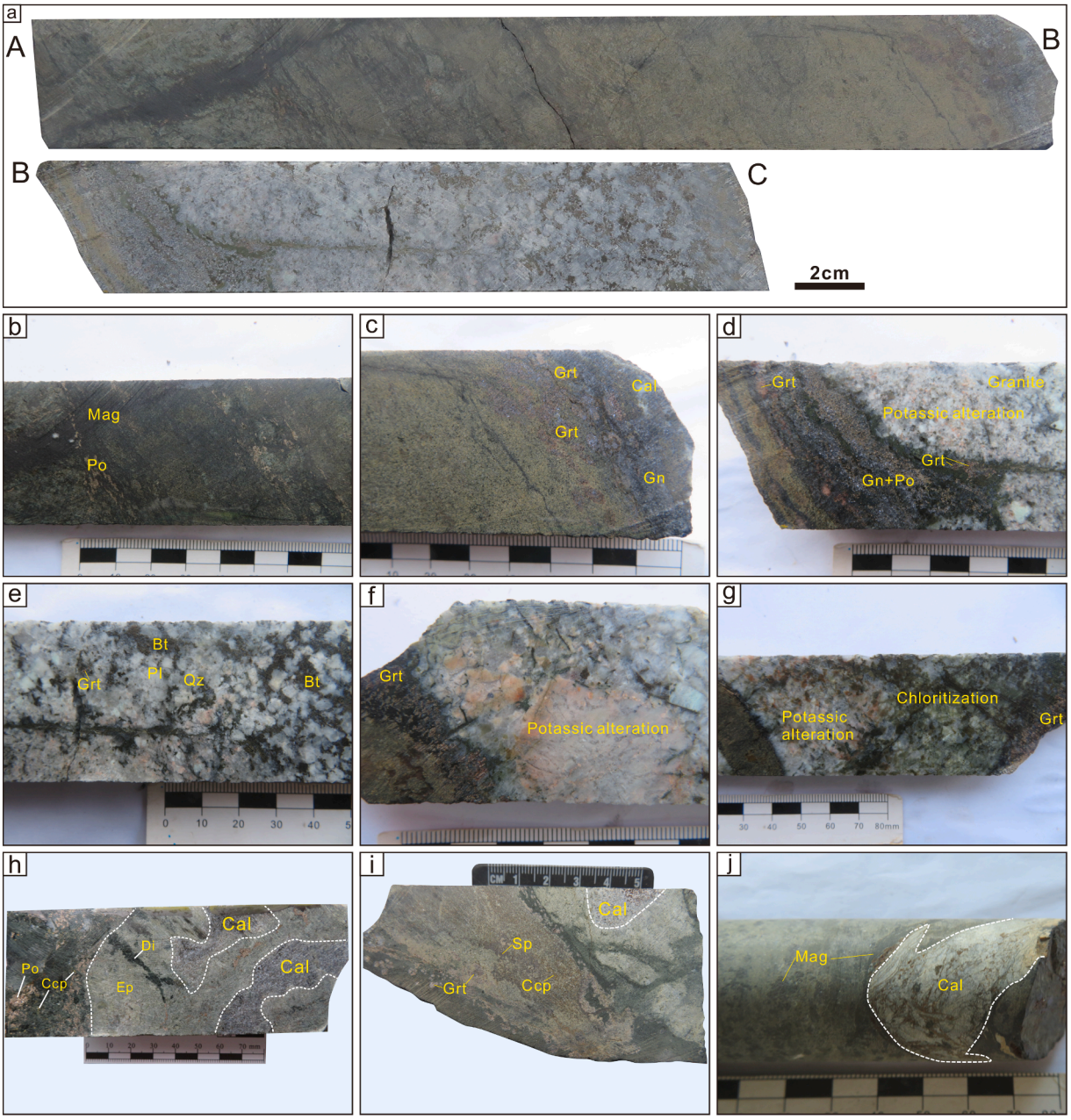

Fig. 4. Representative photographs of samples associated with skarn from the Huogeqi No. 1 and No. 2 deposit. (a–g) Metasomatic contact between the granitoid and skarn. (h–j) Incomplete metasomatism of carbonate remains in skarn. Abbreviations: Mag = magnetite; Py = pyrite; Sp = sphalerite; Gn = galena; Po = pyrrhotite; Ccp = chalcopyrite; Grt = garnet; Di = diopside; Cal = calcite; Bt = biotite; Pl = plagioclase; Qz = quartz.

quartzite, slate, diopside-tremolite rock and marble. The contact relationship between magnetite-bearing tremolite and chalcopyrite-bearing quartzite, as well as with Pb-Zn-bearing slate, is characterized by NW-trending fracture zones filled by calcite (Fig. 1d) (Bao et al., 2021). The stratiform and lensoid-shaped Fe ore bodies (Fig. 2a) comprise coarse-grained disseminated, stratiform, fine-grained dense disseminated and massive (Fig. 2b, 3) Fe ore. Coarse-grained magnetite occurs either as subhedral grains or as aggregates in the diopside-tremolite rocks, or as interstitial space fill between garnets (Fig. 2b, 3a). Fine-grained magnetite together with tremolite and stratified quartz constitute stratiform magnetite ores (Fig. 3b, 5f, g). Fine-grained dense disseminated ores are mainly composed of magnetite, skarn minerals (garnet, tremolite, and diopside), and calcite (Fig. 3c, 5c–e). Magnetite occurs as inclusions in garnet, tremolite, and calcite, and at the contact zone between garnet and calcite (Fig. 5c, d), and diopside and garnet (Fig. 5e). In the massive Fe ore, magnetite is distributed between calcite and in mineral fractures, indicating hydrothermal mineralization (Fig. 5h). The main ore minerals include magnetite, with lesser amounts of galena, sphalerite, pyrrhotite, and chalcopyrite. Gangue minerals include diopside, tremolite, quartz, garnet, and calcite (Figs. 3, 5).

Mineral alteration can be observed in the drill core samples of the No. 1 and No. 2 deposits (Figs. 2–4). In the No. 1 deposit to the south, the contact zone between the granitoid and the skarn can be observed in drill core, where skarn minerals (garnet, diopside and tremolite), ore minerals (magnetite, galena and pyrrhotite) and calcite are developed, and the granitoid shows potassic alteration and chloritization (Fig. 4a–g). In addition, some metasomatic structures, such as marble residue, was observed (Fig. 4h–j). The boundary of the carbonate rocks is curved (Fig. 4h–j) with magnetite developed around (Fig. 4j), indicating hydrothermal alteration.

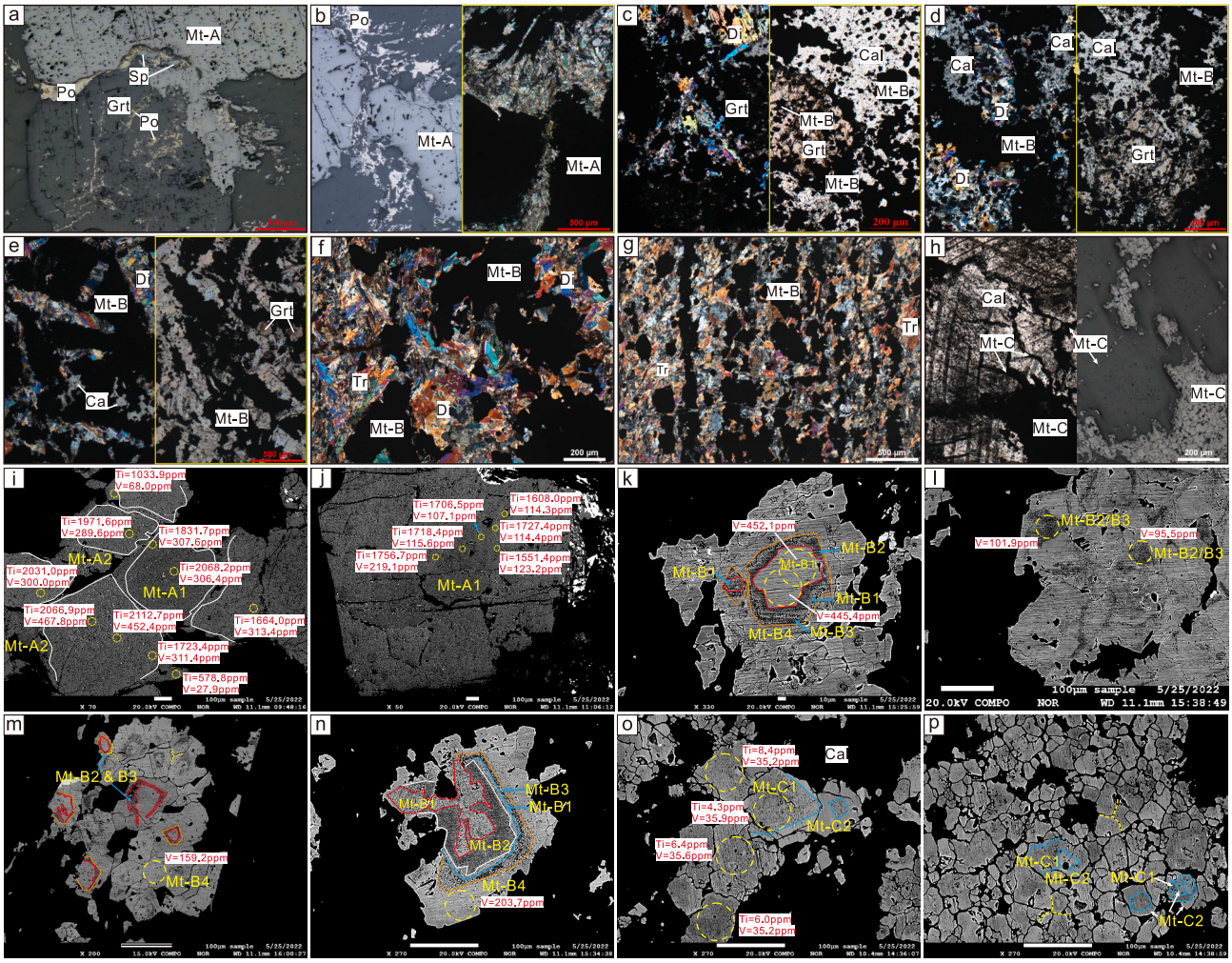

Fig. 5. Photomicrographs of type Mt-A (a, b), Mt-B (c–g) and Mt-C (h) magnetite and (i–p) BSE images of magnetite with some of the images showing Ti and V contents. The yellow dashed circles are the positions of LA-ICP-MS trace element analyses. Abbreviations: Mt = magnetite; Sp = sphalerite; Po = pyrrhotite; Ccp = chalcopyrite; Grt = garnet; Di = diopside; Tr = tremolite; Cal = calcite. (For interpretation of the references to colour in this figure legend, the reader is referred to the web version of this article.)

3. Samples and analytical methods

All samples were collected from the No. 1 and No. 2 deposits. Eleven representative magnetite samples were collected from drill cores and the No. 2 open-cast deposit (Fig. 2b, 3). Five of these samples were selected for EMPA mapping and trace element analysis of magnetite and U-Pb dating of associated garnets. Representative zircons were selected from the granitoid sample collected from drill cores of the No. 1 deposit (Fig. 4) for in-situ U-Pb dating.

3.1. U-Pb dating of garnet and zircon

In-situ garnet U-Pb dating in polished thin sections was done at the Wuhan Sample Solution Analysis Technology Co. Ltd. (Wuhan, China). The analyses were carried out on a 193 nm ArF excimer laser ablation system (GeoLas HD) and an Agilent 7900 ICP-MS for the in-situ micro-analyses (i.e., LA-ICP-MS). The beam diameter was set at 44 μm, and the frequency of the beam was 5 Hz. Detailed analytical methods are available in Liu et al. (2008). Recent studies have demonstrated that the water–vapor assisted LA-ICP-MS method can significantly reduce the matrix effect and obtain accurate U-Th-Pb age corrected by a glass NIST 610 standard or a zircon 91,500 standard (Luo et al., 2019; Luo et al., 2020; Luo et al., 2021). Thus, the zircon standard (91500) was used for in-situ garnet U-Pb dating and as a standard for mass discrimination and U-Pb isotope fractionation (e.g., Chen et al., 2021; Jiang et al., 2021). The trace elements of garnets were calibrated using the glass standard NIST 610, combined with internal standardization (Si).

U-Pb dating of zircons was conducted by using a 193 nm GeoLasPro and Agilent 7900 ICP-MS with a laser spot size of 32 μm at the Wuhan Sample Solution Analysis Technology Co. Ltd. (Wuhan, China). Argon was used as the make-up gas and mixed with the carrier gas via a T-connector before entering the ICP. Zircon 91,500 and glass NIST610 were used as external standards for U-Pb dating and trace element calibration, respectively.

Off-line data processing for garnet and zircon dating was performed using the ICPMSDataCal_version 10.9 software (Liu et al., 2008). Concordia diagrams and weighted mean calculations were prepared using Isoplot/ Ex_ver 4.1(Ludwig, 2010).

3.2. Trace element analysis of magnetite

Trace element analyses of magnetite were conducted by LA-ICP-MS at the Wuhan Sample Solution Analysis Technology Co. Ltd. (Wuhan, China). Detailed operating conditions for the LA-ICP-MS instrument and data reduction are the same as those described by Liu et al. (2008). Laser sampling was performed with GeolasPro laser ablation system, using an Agilent 7500e ICP-MS instrument to acquire ion-signal intensities. Helium was used as the carrier gas and argon as the make-up gas mixed

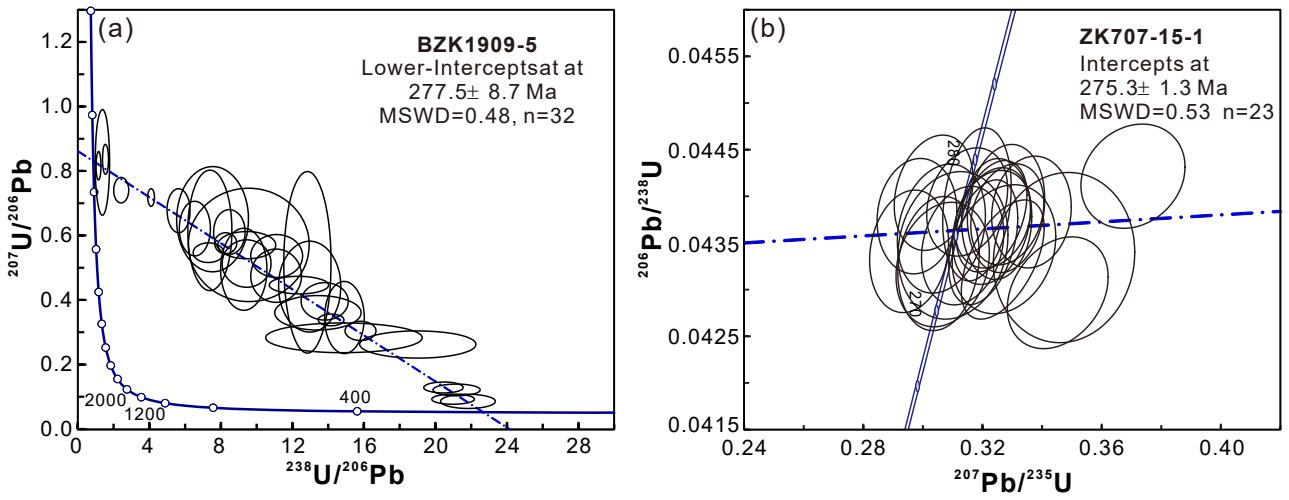

Fig. 6. (a) Garnet U-Pb Tera-Wasserburg concordia diagram. (b) Zircon U-Pb concordia diagram.

with the carrier gas via a T-connector before entering the ICP. The laser spot size was 44 μm in diameter with frequency at 5 Hz. Trace element contents of magnetite were calibrated against various reference materials (NIST 610, BHVO-2G and BCR-2G) (Liu et al., 2008). Each analysis includes a background acquisition of approximately 20–30 s followed by 50 s of data acquisition from the sample. Offline data of magnetite were processed using the software ICPMSDataCal (Liu et al., 2008).

3.3. SEM and element mapping of magnetite

Backscattered electron (BSE) image was carried out at Wuhan SampleSolution Analytical Technology Co., Ltd., using a Zeiss Supra 55 field

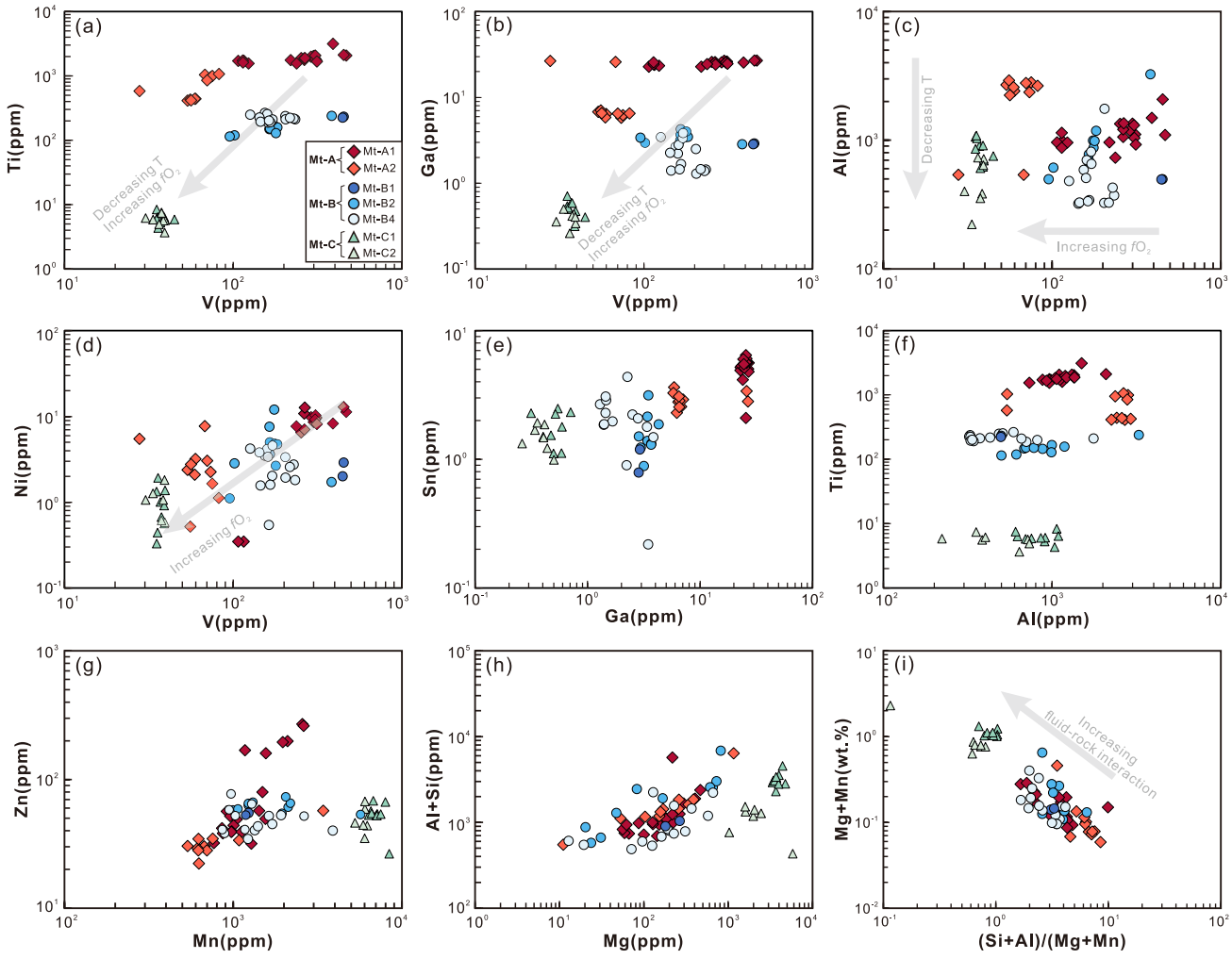

Fig. 7. Binary plots of trace elements in different magnetite types.

emission scanning electron microscope (SEM, JSM-IT100, Japan Electron Optics Laboratory Co., Ltd., Tokyo, Japan) coupled with a cathodoluminescence detector. The BSE images were taken under an accelerating potential of 20 kV, a temperature of 20 °C, and an image acquisition time of 35 s/sheet.

Electron microprobe element mapping of magnetite was completed by using JXA-8230 of JEOL electron microprobe at Wuhan Sample Solution Analytical Technology Co., Ltd. (Wuhan, China). The voltage and current analyzed are 20 kV and 20nA with a beam diameter of 0.5 μm.

4. Results

4.1. U-Pb garnet and zircon geochronology

The magnetite occurs between the garnet grains (Fig. 3a) and shows a symbiotic relationship with garnet (Fig. 5a, c, d), indicating that the hydrothermal garnet coexists with magnetite. A total of 32 LA-ICP-MS analyses were conducted on the garnet, of which the data are available in Supplementary Table S1. The garnet shows variable U contents (0.88 to 33.95 ppm, average = 10.86 ppm) and Th/U mass ratios ranging from 0.13 to 0.88. The U-Pb data indicate a Tera-Wasserburg U-Pb lower intercept age of 277.5 ± 8.7 Ma (MSWD = 0.48; n = 32; Fig. 6a).

Twenty-three spot analyses of zircon from Huogeqi granitoid sample (ZK707-15–1) were conducted by LA-ICP-MS, of which the data are available in Supplementary Table S2. The analyzed zircon grains have Th/U mass ratio ranging from 0.19 to 0.40 and concordant $^{206}Pb/^{238}U$ ages ranging from 278.9 to 271.2 Ma. These age results yield a weighted mean $^{206}Pb/^{238}U$ age of 275.3 ± 1.3 Ma (MSWD = 0.53; n = 23; Fig. 6b), which is interpreted to be the emplacement age of granitoid.

4.2. Petrography of magnetite

By observing mineral assemblages and textural of magnetite in microscope and BSE images, three types (Mt-A, Mt-B and Mt-C) were identified in the Huogeqi Fe orebody. Mt-A, Mt-B and Mt-C are further subdivided into two, four and two subtypes, respectively.

Mt-A occurs as idiomorphic grains with a diameter of 500–3000 μm in disseminated coarse self-shaped magnetite ore, coexisting with diopside, tremolite, garnets, pyrrhotite and sphalerite. Mt-A replaced the early garnet, and both Mt-A and garnet are replaced by pyrrhotite and sphalerite that occur in voids between and within magnetite and garnet (Fig. 5a, b). Mt-A has some pores and fissures, whereas some rotund pyrrhotite occurs as inclusions in Mt-A (Fig. 5a, b, i, j). Furthermore, two generations of Mt-A can be identified in the BSE image, including sub- to euhedral magnetite Mt-A1 with minor cavities and cracks (Fig. 5j), and Mt-A2, which crystallized around Mt-A1 and contains more cavities and cracks (Fig. 5i) compared to Mt-A1.

Mt-B occurs in stratiform and fine-grained dense disseminated magnetite-tremolite ore (Fig. 3b, c), and coexists with skarn minerals (e.g., garnet, diopside and tremolite) and calcite (Fig. 5c–g). Sub- and anhedral Mt-B has a typical triple-junction texture and are partially replaced by chalcopyrite, pyrite and pyrrhotite. Mt-B can be further subdivided into four generations (Fig. 5k–n). Mt-B1 occurs in the magnetite core and between Mt-B2 and Mt-B3, has a bright BSE signal, with few cavities (Fig. 5k, m), or which some are irregular needle-like (Fig. 5m). Mt-B2 has a dark BSE signal and replaced Mt-B1 with sharp and straight boundaries (Fig. 5n). Narrow Mt-B3 surrounds Mt-B2, and is characterized by abundant silicate mineral inclusion and cavities (Fig. 5k, n, 11). Mt-B4 with a few cavities is distributed in the outermost part of Mt-B (Fig. 5k, m, n).

Mt-C coexists with calcite and occurs as sub- to anhedral grains or as aggregates in massive magnetite ore (Fig. 5h). Mt-C is characterized by a triple-junction texture and core-rim texture, and can be further subdivided into Mt-C1 and Mt-C2. Mt-C1 occurs as porous subhedral grains whereas Mt-C2 as a rim around Mt-C1 (Fig. 5o, p, 12a, i) with well-defined grain boundaries.

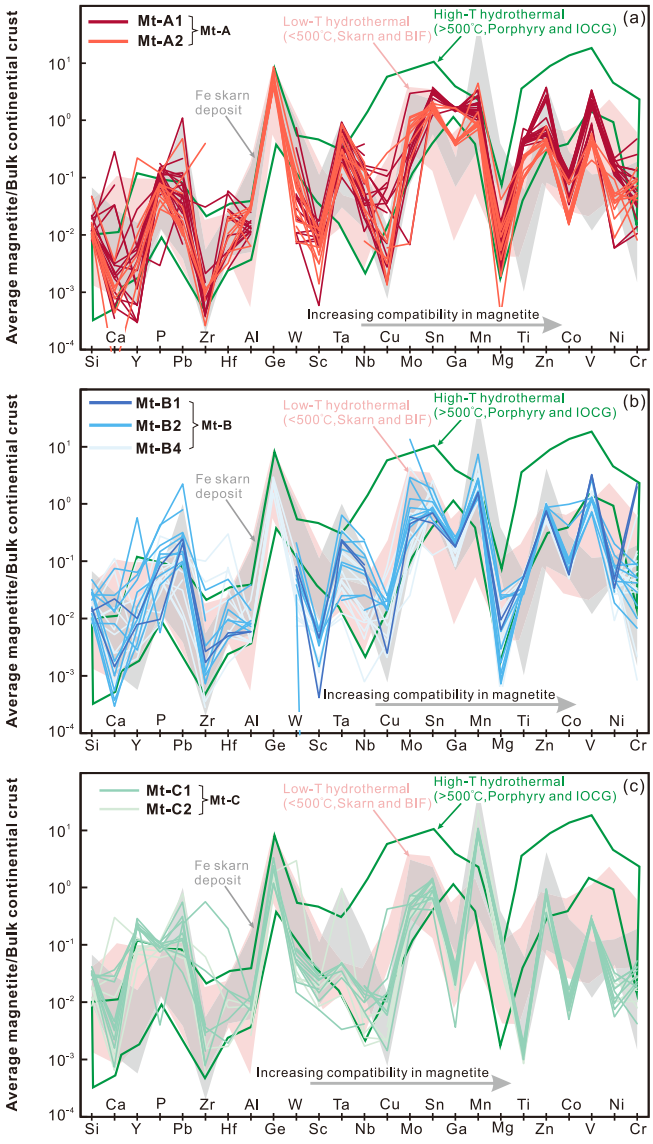

Fig. 8. Multi-element diagrams of average trace element compositions for magnetite from the Huogeqi Fe deposit (after Dare et al., 2014). Normalized values are from Rudnick and Gao (2003).

4.3. Magnetite elemental compositions

The trace element concentrations of the analyzed magnetite from the Huogeqi Fe deposit are presented in Supplementary Table S3 and Figs. 7 and 9. X-ray element mapping (Mg, Al, Si, Mn, Ca, Fe and Ti) carried out on six magnetite grains are shown in Figs. 10 to 12.

Mt-A1 has higher Ca (average 1028 ppm), Mn (average 1363 ppm), Zn (average 78 ppm), Ga (average 25.19 ppm), Sn (average 5.25 ppm), V (average 261 ppm), Ti (average 1881 ppm), Co (average 2.06 ppm) and Ni (average 6.65 ppm), and lower Al (average 1161 ppm) contents than Mt-A2 magnetite. The contents of Mg (average 180 ppm), W (average 0.30 ppm), Nb (average 0.70 ppm), Sc (average 0.17 ppm) and Cr (average 10.69 ppm) in Mt-A1 magnetite are similar to those of the Mt-A2 magnetite (average 189 ppm, 0.22 ppm, 0.56 ppm, 0.15 ppm, and 8.56 ppm, respectively) (Fig. 9).

Mt-B contains four (Mt-B1 to Mt-B4) generations. Since Mt-B3 magnetite is too narrow to obtain trace element analysis data, only the distribution of major elements in Mt-B3 magnetite are shown in the

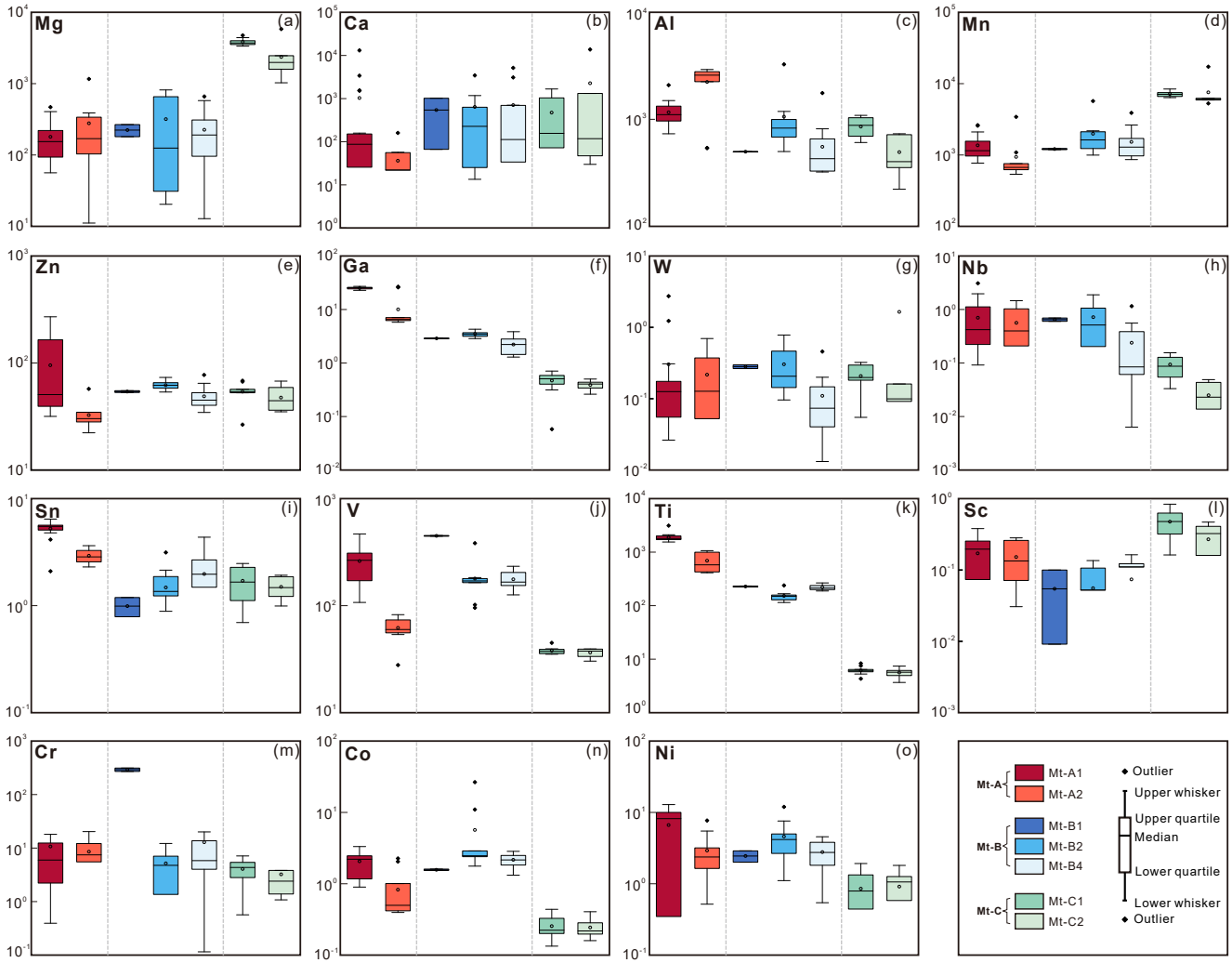

Fig. 9. Box and whisker plots of magnetite trace element concentrations from the different magnetite types in the Huogeqi Fe deposit.

wavelength-dispersive X-ray maps (Fig. 11). The average concentrations of Mg and Ti show a decreasing trend from Mt-B1 to Mt-B2, then increasing from Mt-B2 to Mt-B4 (Fig. 9a, k). From Mt-B1 through Mt-B2 to Mt-B4, the average Al, Mn, Co and Ni contents first increase and then decrease (Fig. 9c, d, n, o). The average Ca, W, Nb and V concentrations show a gradually trend of decreasing values from Mt-B1 to Mt-B4 (Fig. 9b, g, h, j), while the average Sn and Sc contents increase gradually (Fig. 9i, l). Mt-B1, Mt-B2 and Mt-B4 have similar average Zn and Ga contents (Fig. 9e, f).

Compared to Mt-C2 magnetite, Mt-C1 magnetite has higher Mg (average 3852 ppm), Ca (average 472 ppm), Al (average 854 ppm), W (average 0.21 ppm), Nb (average 0.094 ppm), Sc (average 0.48 ppm) and Cr (average 4.07 ppm) contents. Mt-C1 and Mt-C2 have similar average contents of Mn, Zn, Ga, Sn, V, Ti, Co and Ni (Fig. 9).

The positive correlations between Ti and V, Ni and V, Ga and V, Ti and Al, and Zn and Mn are shown in the binary diagrams (Fig. 7). The magnetite trace element contents show generally decreasing trends of Ga, Nb, Sn, Ti, and Ni contents but fluctuating trends of Mg, Ca, Al, Mn, W, V, Sc, Cr and Co contents from the disseminated coarse self-shaped magnetite ores (Mt-A) to the massive magnetite ores (Mt-C) (Fig. 9).

The major elements of Mt-A1 and Mt-A2 magnetite are, except for Ti, evenly distributed. The Ti content in Mt-A1 is higher (>0.1 wt%) than in Mt-A2 (Fig. 10). Mt-B1 has slightly lower Mg, Si, and Mn contents than Mt-B2. Both Mt-B1 and Mt-B2 show lower Mg, Si, Mn, and Fe contents than Mt-B3. In contrast, Mt-B3 has lower Fe and higher Mg, Si and Mn contents, and contains many silicate inclusions as shown by Si and Mg element maps. Mt-B4 has the lowest Mg, Si and Mn contents among the four Mt-B types. The contents of Al, Ca and Ti are similar in all four Mt-B generations (Fig. 11). Mt-C1 magnetite shows higher Mg, Al, Si and Mn contents than Mt-C2 whereas the Ca, Fe, and Ti contents are similar in Mt-C1 and Mt-C2 (Fig. 12).

5. Discussion

5.1. Timing of Fe mineralization

The textural relationship between magnetite and garnet indicates that they were coexisting and related to the same hydrothermal activities (Fig. 5a, c–e). The crystallization age, therefore, represents the formation age of magnetite. In this study, LA-ICP-MS U-Pb dating of magnetite-bearing garnets yields an age of 277.5 ± 8.7 Ma (Fig. 6a) and the zircon U-Pb age of the granitoid that is in contact with skarn yields an age of 275.3 ± 1.3 Ma (Fig. 6b). The age of hydrothermal garnet is within error with the zircon age, indicating that the granitoid and hydrothermal event are coeval. This is supported by the alteration of the granitoid-skarn contact observed in drill core (Fig. 4). Zhong et al. (2015) suggested that the $^{39}Ar/^{40}Ar$ age (271.4 ± 29.5 Ma) of magnetite-bearing tremolite-diopside rocks represents the peak metamorphic age, which is consistent with the emplacement age of the widely distributed Permian intrusive rocks. Permian intrusive rocks are

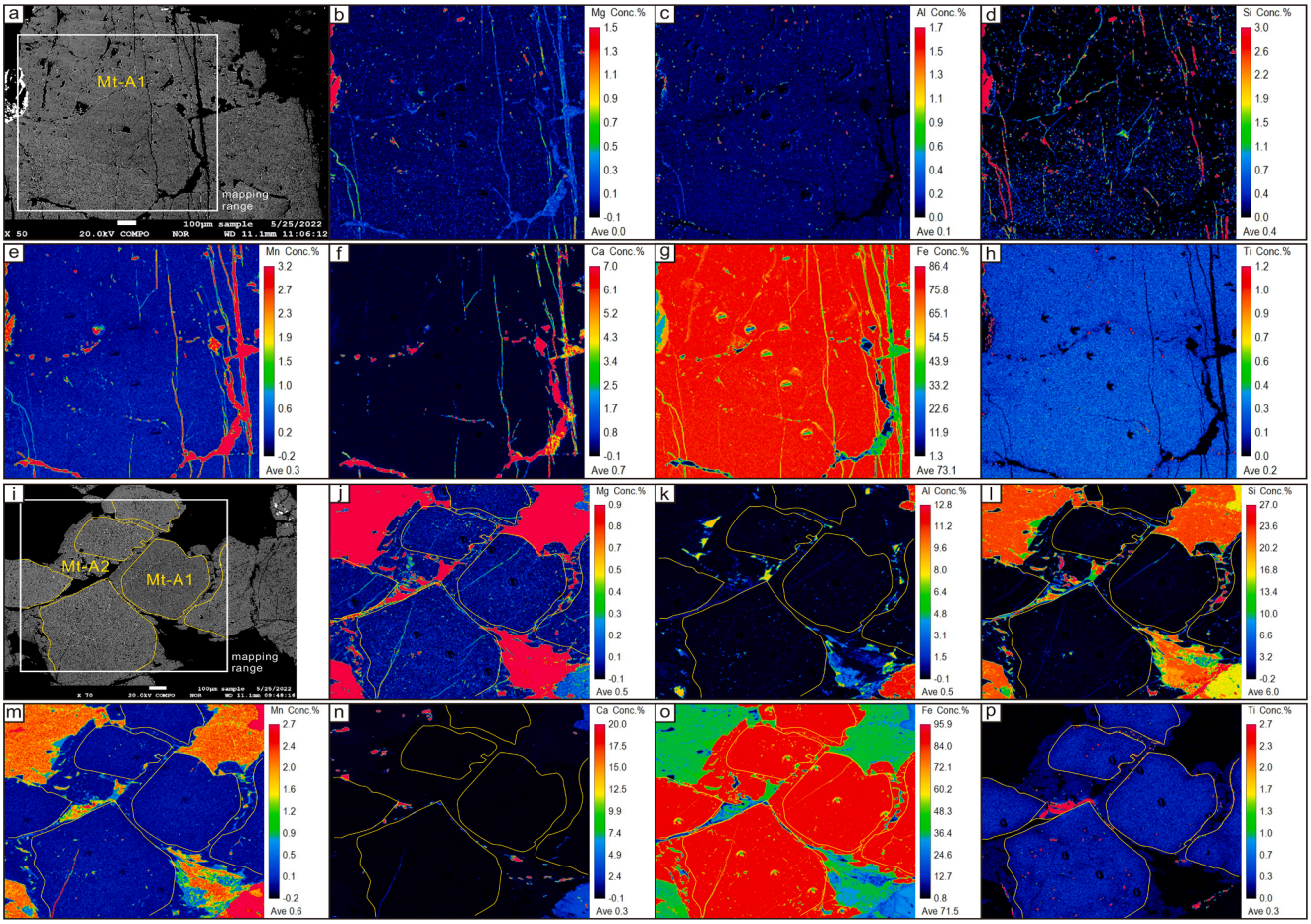

Fig. 10. (a, i) BSE images of Mt-A grains in the Huogeqi Fe deposit. (b–h, j–p) Corresponding wavelength-dispersive X-ray maps of selected elements (Mg, Al, Si, Mn, Ca, Fe and Ti) of Mt-A.

prevailing in the Huogeqi orefield and include the gabbro-diorite (274 ± 1 Ma, Pi et al., 2010), quartz diorite (270 ± 4 Ma and 273 ± 1 Ma, Su, 2019) and granodiorite (272 ± 2 Ma, An, 2019). These geochronological data suggest that there was large-scale magmatic-hydrothermal activity in the Huogeqi area, which is coeval with the timing of Fe mineralization in the Huogeqi deposit. This indicates that the Fe mineralization is related to this tectonic-hydrothermal event, which was triggered by the northwest rollback of the Enger Us slab in the Permian (270–285 Ma) (Zheng et al., 2021).

5.2. Physicochemical conditions of magnetite formation

All magnetite samples display trace-element patterns (Fig. 8) that indicate a common source for different types of magnetite. However, the contents of specific elements (Ti, V, Mn, and Ga) in magnetite are affected by the fluid physicochemical factors (composition, temperature, and oxygen fugacity), the co-precipitation of other minerals, and fluid-rock interactions (Dare et al., 2014; Nadoll et al., 2014), do vary for the different magnetite types.

The temperature is regarded as a major factor that impacts the composition of magnetite by controlling element partition coefficients (McIntire, 1963). Generally, the Ti content in hydrothermal magnetite shows a positive correlation with temperature (Dare et al., 2012; Nadoll et al., 2012). At the Huogeqi Fe deposit, the gradual drop in Ti contents from Mt-A through Mt-B to Mt-C, therefore, suggests progressive cooling from the disseminated coarse self-shaped magnetite ore to massive magnetite ore. This interpretation is supported by a binary diagram of Ti and V contents (Fig. 7a) and (Ti + V) vs. (Al + Mn) diagram (Fig. 13f). A similar decreasing trend of the Ga and Sn contents as the Ti content implies that the Ga and Sn contents are also governed by temperature (Fig. 9f, i). Furthermore, since Zn and Mn partition preferentially into magnetite under low-temperature conditions in Cl-rich fluids (Ilton and Eugster, 1989), the positive relationship between Zn and Mn (Fig. 7g), and the increasing of Mn content (Fig. 9d) from Mt-A to Mt-C also confirms that the formation temperature of Huogeqi magnetite decreased from Mt-A to Mt-C.

Oxygen fugacity (fO_2) also affects the magnetite composition as it controls element partition coefficients (Hu et al., 2020). The V content in magnetite is sensitive to a fO_2 change of the hydrothermal fluid because the compatibility of V in magnetite depends on the different V valence states, which depends on fO_2 (Nielsen et al., 1994; Righter et al., 2006), i.e. V is incompatible under high fO_2 (Toplis and Corgne, 2002; Sievwright et al., 2017). The significant decrease in V content from high-Ti Mt-A to low-Ti Mt-C indicates that the fO_2 increased from the disseminated coarse self-shaped magnetite ore (Mt-A) to the massive magnetite ore (Mt-C) (Fig. 7a–d, 9j).

Magnetite characterized by low Ti and V contents and relatively high Mg and Mn contents have been reported to occur in skarn deposits (Nadoll et al., 2015). Furthermore, magnetite that formed by fluid-rock interaction would inherit some geochemical features of the fluid and wall rock (Nadoll et al., 2014; Liu et al., 2019a, Liu et al., 2019b). The positive relationship between (Al + Si) and Mg (Fig. 7h) reflecting that magnetite from Huogeqi have undergone a certain degree of fluid-rock interaction (Liu et al., 2019a, Liu et al., 2019b). The Mt-A and Mt-B magnetite have higher (Si + Al)/(Mg + Mn) ratios and lower (Mg + Mn) values than Mt-C (Fig. 7i), which suggests that the lower degree of

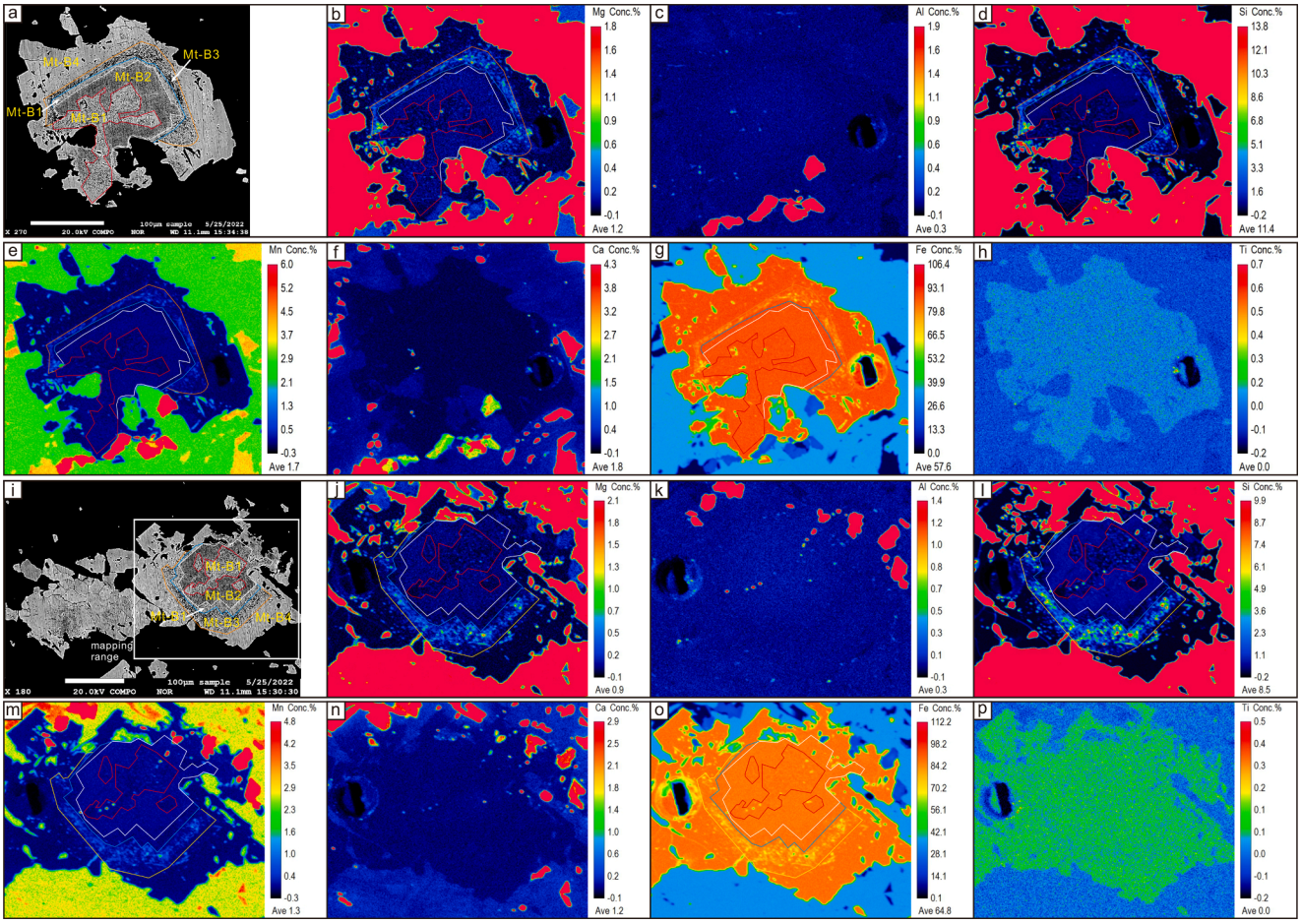

Fig. 11. (a, i) BSE images of Mt-B grains in the Huogeqi Fe deposit. (b–h, j–p) Corresponding wavelength-dispersive X-ray maps of selected elements (Mg, Al, Si, Mn, Ca, Fe and Ti) of Mt-B.

fluid-rock interaction (Dong et al., 2021). In contrast, the higher Mg, Mn and lower Ti, V in Mt-C that coexisted with calcite (Fig. 5h, 9) may have been influenced by extensive fluid-rock interaction in Cl-rich fluids (Liu et al., 2019a, Liu et al., 2019b), which is further supported by higher Mn content of calcite occurring near Mt-C magnetite (Fig. 12m).

In summary, the physical–chemical properties of hydrothermal fluids do affect the formation of Huogeqi magnetite comprehensively. Conversely, the elemental composition of magnetite can indirectly reflect the characteristics of hydrothermal fluids during magnetite precipitation. The difference elemental concentrations in Huogeqi magnetites indicates that the ore-forming fluid gradually evolves from a high temperature, low fO_2, and fluid-rock ratio to a relatively low temperature, high fO_2, and high fluid-rock ratio.

5.3. Origins of the Huogeqi magnetites

The magnetite composition can be used to constrain its origin (Dupuis and Beaudoin, 2011; Dare et al., 2014; Wen et al., 2017; Chen et al., 2020). Based on the petrographic observation and composition of Huogeqi magnetite, a hydrothermal origin appears to be more likely than a magmatic origin. This is based on the following: (1) Magnetite commonly co exists with skarn minerals such as garnet, tremolite (Fig. 5a–g). The retrograde alteration minerals and magnetite replaced the prograde skarn minerals (Fig. 5c, d), after which the magnetite was replaced by sulfides (Fig. 5a, b). In addition, residual metasomatic carbonate minerals can be seen in the gap of precipitated magnetite (Fig. 5c, d), and some fine magnetite precipitated in the cracks in the carbonate minerals (Fig. 5h). These petrographic characteristics indicate a hydrothermal origin for Huogeqi magnetite. (2) Magmatic magnetite precipitated at higher temperature commonly has higher trace element contents, which would result in a depletion in Fe contents (< ~65 wt%) of the magmatic magnetite (Nadoll et al., 2014; Wen et al., 2017). All magnetite types from the Huogeqi deposit show low lithophile elements (e.g., Ti and V) contents and high Fe contents (> ~75 wt%, Fig. 13c), which is inconsistent with magmatic magnetite. (3) Most of the Huogeqi magnetite have lower Ti and V contents and higher Ni/Cr ratios compared to magmatic magnetite, and plot into the field of hydrothermal magnetite in the V vs. Ti and Ti vs. Ni/Cr discrimination diagrams (Fig. 13a, b).

The multi-element spider diagrams show that the Huogeqi magnetite is geochemically similar as a low temperature hydrothermal magnetite (T < 500 °C, magnetite from skarn and BIF) and a hydrothermal magnetite from a Fe skarn deposit, especially with regards to Sn, Ga, Zn, Zr, and Nb (Fig. 8). Furthermore, the Huogeqi magnetite plots in the skarn field in the Ti + V vs. Ni/(Cr + Mn) diagram (Fig. 13e), which is consistent with those of the origin from the Fe skarn deposits. The high (Ti + V) and (Ca + Al + Mn) values of Mt-A (Fig. 13d) indicate that the high-Ti Mt-A may have a magmatic-hydrothermal origin (Liang et al., 2020).

5.4. Evolution of the Huogeqi magnetite

The majority of skarn- and IOCG-related magnetite has been extensively modified by dissolution of primary magnetite and precipitation of secondary magnetite with sharp contact boundaries (Hu et al., 2014; Hu et al., 2015; Hu et al., 2020; Liang et al., 2020). Magnetite that has been

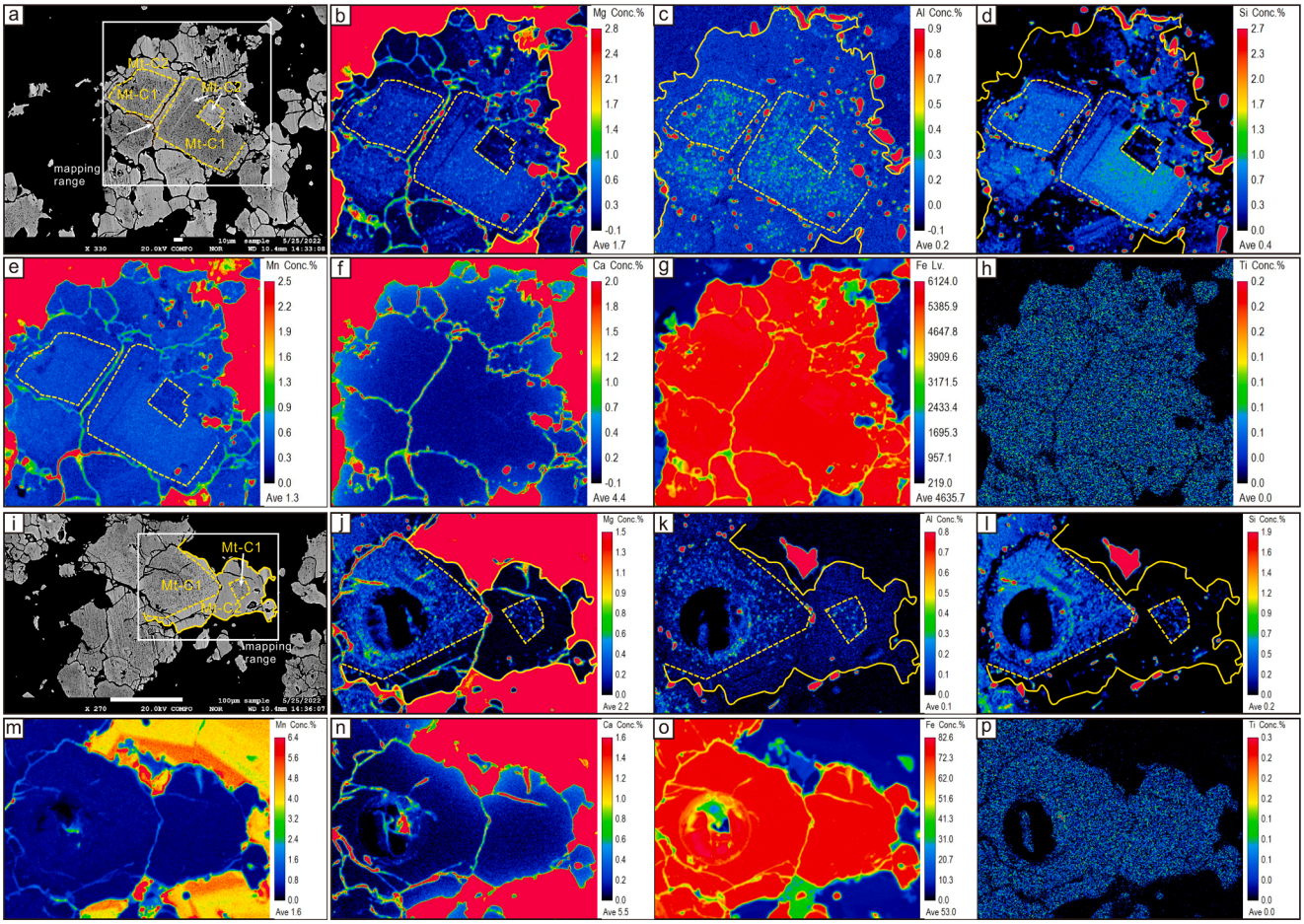

Fig. 12. (a, i) BSE images of Mt-C grains in the Huogeqi Fe deposit. (b–h, j–p) Corresponding wavelength-dispersive X-ray maps of selected elements (Mg, Al, Si, Mn, Ca, Fe and Ti) of Mt-C.

formed through a dissolution and reprecipitation process (DRP) displays different trace element contents (e.g., Si, Mg, Al) compared to the primary magnetite (Hu et al., 2014; Liang et al., 2020; Zhao et al., 2022). The early high-Ti Mt-A exhibits a relatively uniform texture (Fig. 10a, i) and uniform Si, Mn, Mg and Al contents without sharp grain boundaries (Fig. 10). This indicates that Mt-A was not modified by DRP, which is confirmed by the consistent (Si + Ca + Al + Mg + Mn) contents of Mt-A1 and Mt-A2 (Fig. 14d). The precipitation of Mt-A2 with relatively low Ti and V contents around Mt-A1 with higher Ti and V contents implies precipitation of Mt-A2 at a lower temperature and higher fO_2 (Fig. 14a).

The Mt-B displays a typical 120° triple junction texture (Fig. 5m) indicating magnetite recrystallization as the result of high-temperature annealing (Ciobanu and Cook, 2004) and fluid-assisted replacement (Nakamura and Watson, 2001). The three Mt-B types (Mt-B1, Mt-B2 and Mt-B4) show different Fe and trace element contents (Figs. 9, 14d), and different (Si + Ca + Al + Mg + Mn) values (Fig. 14d), which indicate that Mt-B was probably formed by fluid-assisted recrystallization (Hu et al., 2023). Porous Mt-B2 has a dark BSE signal and replaces Mt-B1. Mt-B1 is also replaced by porous Mt-B3 that contains silicate mineral inclusions (Fig. 11). Mt-B3 and Mt-B2 show higher Mg, Si, and Mn contents and lower V contents than Mt-B1 (Figs. 5, 11), which indicate a lower temperature and higher fO_2 conditions (Nadoll et al., 2014; Liang et al., 2020). The textural and geochemical characteristics of Mt-B1, Mt-B2, and Mt-B3 (Figs. 9, 11) suggest that DRP may have played an important role in their formation. With a slight temperature increase and a slight fO_2 decrease, Mt-B4 was also formed through DRP, which is characteristic by fewer pores and lower Mg, Si and Mn contents and sharp contact with Mt-B2 or Mt-B3 (Fig. 14b). During the DRP of Mt-B1 to Mt-B4, the (Si + Ca + Al + Mg + Mn) value first increases and then decreases whereas the Fe content shows an opposite trend (Fig. 14d).

Finally, for the low-Ti Mt-C with triple-junction texture (Fig. 12a), the sharp contact between Mt-C1 and Mt-C2, and the lower Mg, Si, Al, and Mn contents (Figs. 9, 12, 14d) and higher Fe contents (average Fe content of Mt-C1 is 74.8 wt%, average Fe content of Mt-C2 is 75.6 wt%) of Mt-C2, indicate that Mt-C2 was also formed via DRP (Fig. 14c).

5.5. Implications for ore deposit formation

The textural and geochemical characteristics of magnetite described in this study indicates that the Huogeqi Fe deposit can be classified as a skarn-type Fe deposit. This is based on (1) the presence of typical skarn minerals (Figs. 2–5), (2) the local occurrence of a metasomatic contact between the granitoid and skarn (Fig. 4a–g), (3) the incomplete metasomatism of carbonate remains (Fig. 4h–j), and (4) the trace element composition and the enrichment of light Fe isotopes in magnetite (Bao et al., 2021), which are typical for hydrothermal magnetite in skarn deposit.

Generally, skarn Fe-Cu polymetallic deposits are related to calc-alkaline magmatism (Chen and Xiao, 2014). In a back-arc extensional setting triggered by the rollback of the Enger Us slab (Zheng et al., 2021) during Early-Middle Permian, heat input through asthenosphere upwelling caused partial melting of the crust to form A2-type granite, felsic magmatic rocks with calc-alkaline features (Liu et al., 2017), and the Qagan Qulu ophiolite (Zheng et al., 2014). These felsic magmatic rocks with calc-alkaline features could be related to regional skarn Fe-Cu polymetallic mineralization. In the process of magmatic emplacement,

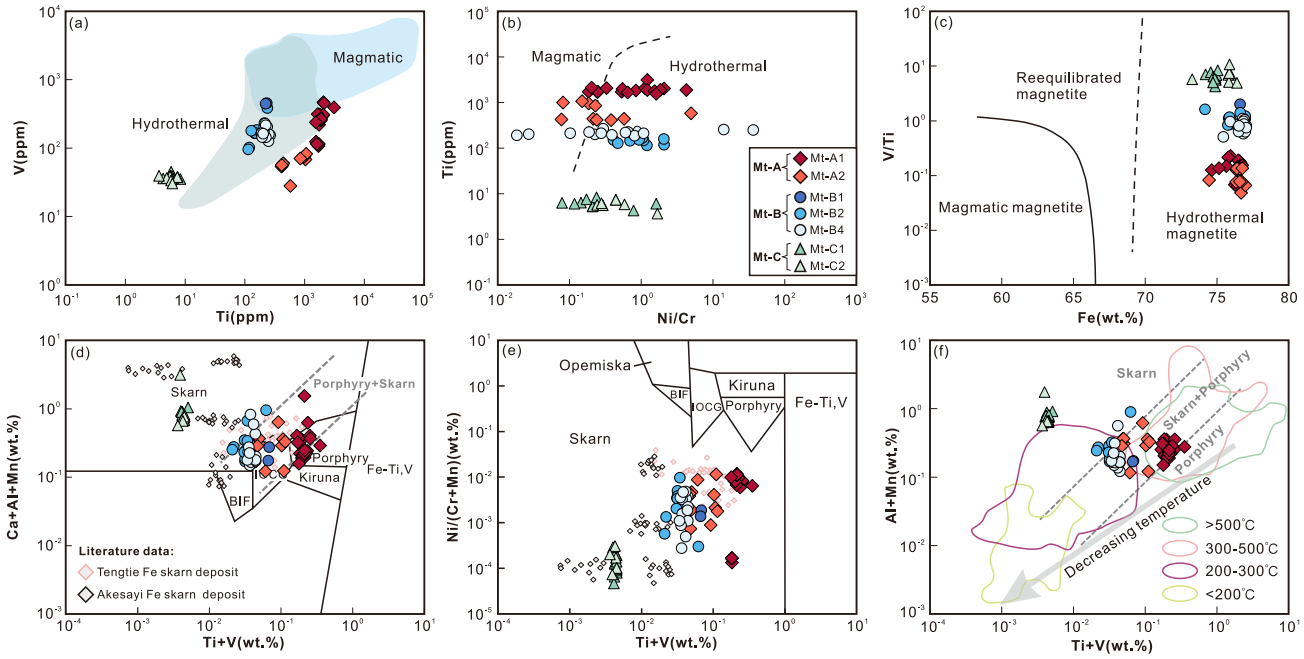

Fig. 13. Genetic discrimination diagram for magnetite in the Huogeqi Fe deposit. (a) Ti vs. V (Chen et al., 2020), (b) Ni/Cr vs. Ti (Dare et al., 2014), (c) Fe vs. V/Ti (Wen et al., 2017), (d) (Ti + V) vs. (Ca + Al + Mn), (e) (Ti + V) vs. Ni/(Cr + Mn) (Dupuis and Beaudoin, 2011) and (f) (Ti + V) vs. (Al + Mn) (Nadoll et al., 2014). Abbreviations: BIF = banded iron formation; Skarn = Fe skarn deposits; IOCG = Fe-oxide-Cu-Au deposits; Porphyry = porphyry Cu deposits; Kiruna = Kiruna apatite-magnetite deposits; Fe-Ti-V = magmatic Fe-Ti-oxide deposits. Data for Tengtie Fe skarn deposit are from Zhao and Zhou (2015), data for the Akesayi Fe skarn deposit are from Dong et al. (2021).

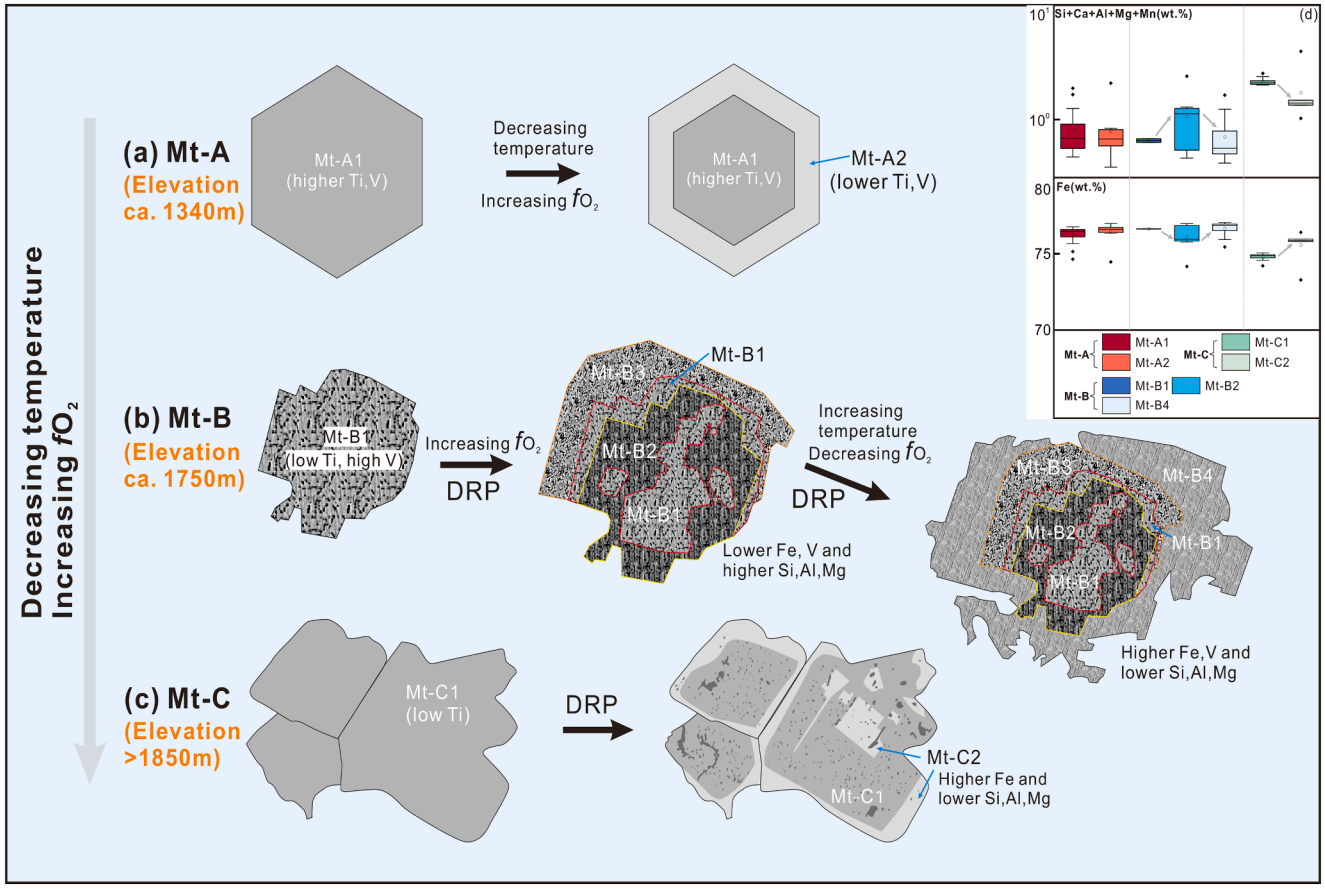

Fig. 14. Schematic diagram showing the textural and geochemical evolution for the magnetite from Huogeqi Fe deposit.

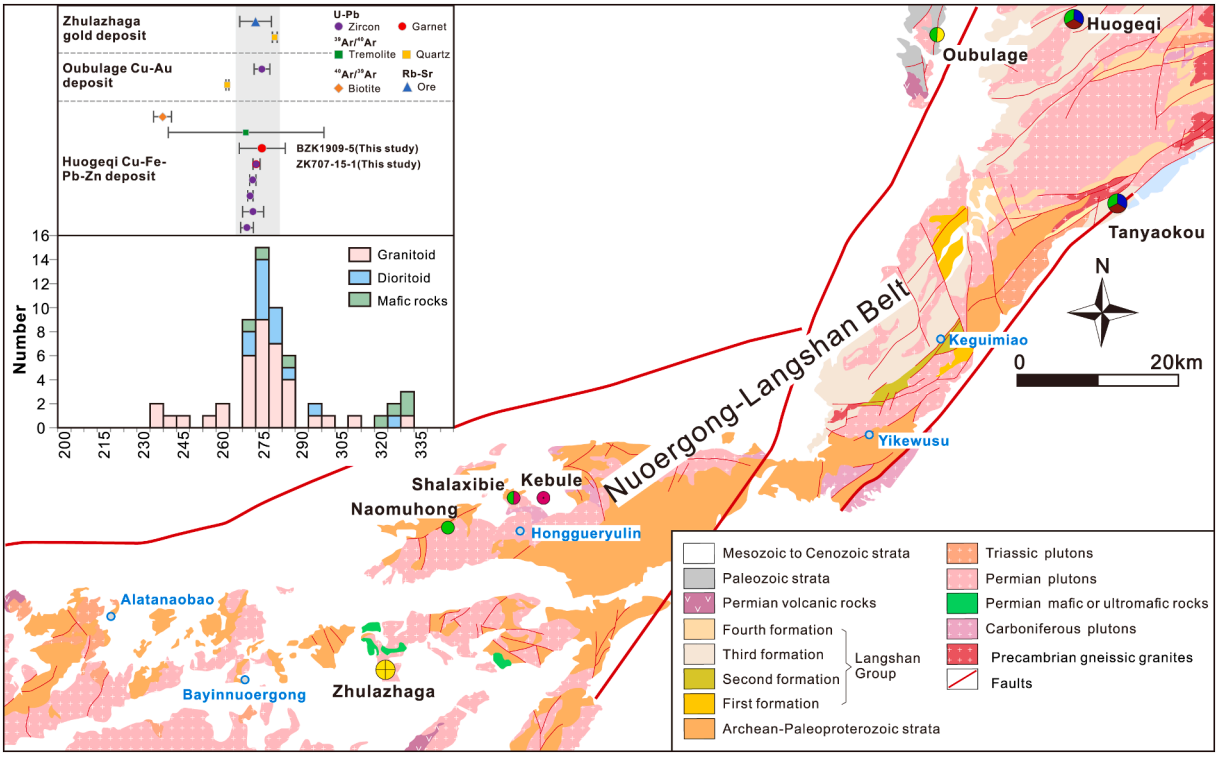

Fig. 15. Geological map of the Nuoergong-Langshan Belt and temporal distribution of metallogenic events and magmatic rocks.

the hydrothermal fluid rose along the NW-trending fault and reacted with the Meso-Neoproterozoic carbonate strata (dolomitic marble and marble) near the fault to form skarnization and Fe mineralization. Magnetite is the dominate Fe-bearing mineral in this deposit. As the temperature of the mineralizing hydrothermal fluid decreased whereas the fO_2 increased, and the fluid-rock reaction increased from deep to shallow, the coarse-grained magnetite ore (Mt-A) with high Ti and V contents was first formed in a deep elevation, then the stratiform and fine-grained dense disseminated magnetite ore (Mt-B) were formed, and the massive magnetite ore (Mt-C) with low Ti and V contents was finally formed in a shallow elevation (Fig. 14).

In addition, strong magmatic-hydrothermal activity in the Nuoergong-Langshan Belt during Late Paleozoic led to the formation of the Oubulage Cu-Au (Li et al., 2010; Wang, 2014), Zhulazhaga Au (Ding et al., 2016), and skarn-type Fe-Cu mineralization, such as Huogeqi Fe deposit, and three Fe-Cu deposits in Hongguyulin area with similar geological characteristics to the Huogeqi Fe deposit (Supplementary Table S4, Fig. 15; Li, 2006; Yang et al., 2018).

6. Conclusions

The Fe mineralization in Huogeqi occurred at 277.5 ± 8.7 Ma, which is coeval with the emplacement age of the mineralized-related granitoid (275.3 ± 1.3 Ma), as well as the regional Fe-Cu-Au mineralization and Early-Middle Permian magmatism in the Nuoergong-Langshan area.

Three magnetite types were identified, including Mt-A (disseminated, coarse-grained, and self-shaped), Mt-B (stratiform and fine-grained dense disseminated), and Mt-C (massive). The mineralizing hydrothermal fluid progressively cooled and the fO_2 gradually increased. Dissolution and reprecipitation of magnetite played a vital role in the formation of Mt-B and Mt-C.

The hydrothermal Huogeqi Fe deposit can be classified as a skarn-type deposit, which is related to late stage Early Permian magmatism.

Declaration of Competing Interest

The authors declare that they have no known competing financial interests or personal relationships that could have appeared to influence the work reported in this paper.

Data availability

Data will be made available on request.

Acknowledgments

This research was jointly supported by the National Natural Science Foundation of China (project number 41772071, 41902090). We sincerely thank Editor-in-Chief Prof. Huayong Chen and the two anonymous reviewers for their constructive comments. We would like to thank the valuable help from Yue Hu, Senlin Yan, Tengfeng Miao and Shuang Wang during the fieldwork.

Appendix A. Supplementary data

Supplementary data to this article can be found online at https://doi.org/10.1016/j.oregeorev.2023.105747.

References

An, S.F., 2019. Geological and Geochemical Characteristics of the Huogeqi Granodiorite in Inner Mongolia and Its Geological Significance. Hebei Geo University, China. Master thesis (in Chinese with English abstract).

Bao, C., 2016. Genesis of the Huogeqi Copper polymetallic deposit in the Inner Mongolia and the regional crustal evolution. China University of Geoscience, China. Doctoral thesis (in Chinese with English abstract).

Bao, C., Chen, Y.L., Zhu, X.K., Zhao, J.X., 2019. Attribution of the Langshan Tectonic Belt: Evidence from zircon U-Pb ages and Hf isotope compositions. Geosci. Front. 10 (2), 539–551.

Bao, C., Zhu, X.K., Gao, Z.F., 2021. Iron isotope constraints on the genesis of magnetite ore in the Huogeqi deposit of Inner Mongolia autonomous region in northern China. Ore Geol. Rev. 133, 104116.

Chen, F.C., Deng, J., Wang, Q.F., Huizenga, J.M., Li, G.J., Gu, Y.W., 2020. LA-ICP-MS trace element analysis of magnetite and pyrite from the Hetaoping Fe-Zn-Pb skarn deposit in Baoshan block, SW China: Implications for ore-forming processes. Ore Geol. Rev. 117, 103309.
Chen, J.H., Wang, Q.F., Shu, Q.H., Weng, W.J., Xu, X.J., Wang, T.Y., Zhang, Q.Z., 2021. Geology and genesis of the Debao Cu polymetallic skarn deposit, southwestern China. Ore Geol. Rev. 131, 104046.
Chen, H.Y., Xiao, B., 2014. Metallogenesis of subduction zone: The progress and future. Earth Sci. Front. 21 (5), 13–22 in Chinese with English abstract.
Ciobanu, C.L., Cook, N.J., 2004. Skarn textures and a case study: the Ocna de Fier-Dognecea orefield, Banat. Romania. Ore Geol. Rev. 24 (3–4), 315–370.
Dare, S.A.S., Barnes, S., Beaudoin, G., 2012. Variation in trace element content of magnetite crystallized from a fractionating sulfide liquid, Sudbury, Canada: Implications for provenance discrimination. Geochim. Cosmochim. Acta 88, 27–50.
Dare, S.A.S., Barnes, S., Beaudoin, G., Méric, J., Boutroy, E., Potvin-Doucet, C., 2014. Trace elements in magnetite as petrogenetic indicators. Miner. Depos. 49 (7), 785–796.
Ding, C.W., Nie, F.J., Jiang, S.H., Liu, Y.F., Cao, Y., 2016. Characteristics and origin of the Zhulazhaga gold deposit in Inner Mongolia. China. Ore Geol. Rev. 73, 211–221.
Dong, R., Wang, H., Li, W.Q., Yan, Q.H., Zhang, X.Y., 2021. The geology, magnetite geochemistry, and oxygen isotopic composition of the Akesayi skarn iron deposit, Western Kunlun Orogenic Belt, Xinjiang, northwest China: Implications for ore genesis. Ore Geol. Rev. 130, 103854.
Dupuis, C., Beaudoin, G., 2011. Discriminant diagrams for iron oxide trace element fingerprinting of mineral deposit types. Miner. Depos. 46 (4), 319–335.
Gao, Z.F., Zhu, X.K., Sun, J., Luo, Z.H., Bao, C., Tang, C., Ma, J.X., 2018. Spatial evolution of Zn-Fe-Pb isotopes of sphalerite within a single ore body: A case study from the Dongshengmiao ore deposit, Inner Mongolia. China. Miner. Depos. 53 (1), 55–65.
Gao, Z.F., Zhu, X.K., Bao, C., Ma, J.X., Sun, J., 2019. Constraints of lead isotopes on regional metallogeny of sediment-hosted sulfide deposits in the Langshan-Zhaertai ore belt, northern China. J. Asian Earth Sci. 184, 103973.
Guo, S., Teng, X.J., Liu, Y., Teng, F., He, P., Tian, J., Wang, W.L., Duan, X.L., 2019. The Age and Potential Provenance Information of Amushan Formation in Wulanaobao Area, Northwestern of Langshan, Inner Mongolia and Its Geological Significance. Earth Sci. 44 (1), 193–205 in Chinese with English abstract.
Hu, X., Chen, H.Y., Beaudoin, G., Zhang, Y., 2020. Textural and compositional evolution of iron oxides at Mina Justa (Peru): implications for mushketovite and formation of IOCG deposits. Am. Mineral. 105, 397–408.
Hu, H., Li, J.W., Lentz, D., Ren, Z., Zhao, X.F., Deng, X.D., Hall, D., 2014. Dissolution–reprecipitation process of magnetite from the Chengchao iron deposit: Insights into ore genesis and implication for in-situ chemical analysis of magnetite. Ore Geol. Rev. 57, 393–405.
Hu, H., Lentz, D., Li, J.W., McCarron, T., Zhao, X.F., 2015. Reequilibration processes in magnetite from iron skarn deposits. Econ. Geol. 110, 1–8.
Hu, X., Xiao, B., Jiang, H., Huang, J., 2023. Magnetite texture and trace element evolution in the Shaquanzi Fe-Cu deposit, Eastern Tianshan, NW China. Ore Geol. Rev. 154, 105306.
Huang, C.K., Bai, Z., Zhu, Y.S., Wang, H.Z., Shang, X.Z., 2001. Copper Deposit of China. Geological Publishing House, Beijing (in Chinese with English abstracts).
Huang, X., Beaudoin, G., 2019. Textures and Chemical Compositions of Magnetite from Iron Oxide Copper-Gold (IOCG) and Kiruna-Type Iron Oxide-Apatite (IOA) Deposits and Their Implications for Ore Genesis and Magnetite Classification Schemes. Econ. Geol. 114 (5), 953–979.
Hui, J., Zhang, K.J., Zhang, J., Qu, J.F., Zhang, B.H., Zhao, H., Niu, P.F., 2021. Middle–late Permian high-K adakitic granitoids in the NE Alxa block, northern China: Orogenic record following the closure of a Paleo-Asian oceanic branch? Lithos 400–401, 106379.
Ilton, E.S., Eugster, H.P., 1989. Base metal exchange between magnetite and a chloride-rich hydothermal fluid. Geochim. Cosmochim. Acta 53, 291–301.
Jiang, X.J., Zheng, Y.Y., Gao, S.B., Yan, J., Kang, Y.M., Jiang, G.W., Liu, J.B., Zhang, Z.L., Chen, X., 2021. In-situ U-Pb geochronology of Ti-bearing andradite as a practical tool for linking skarn alteration and Pb-Zn mineralization: A case study of the Mengya'a deposit. Tibet. Ore Geol. Rev. 139, 104565.
Li, J.J., 2006. Regional Metallogenic System of Alashan Block in Inner Monolia Autonomous Region. China University of Geoscience, China. Doctoral thesis (in Chinese with English abstract).
Li, J.J., Zhai, Y.S., Sang, H.Q., Li, H.M., Zhang, Y.S., Liu, S.Y., Wang, S.G., Sun, Z.P., Liu, X.X., 2010a. Metallogenic epoch of the oubulage copper-gold deposit in the Alashan Area, Inner Mongolia autonomous region. Bull. Mineral. Petrol. Geochem. 29, 323–327 in Chinese with English abstract.
Li, J.J., Zhai, Y.S., Yang, Y.Q., Wang, Y.B., Li, C.D., Cui, L.W., Zhou, H.Y., Liu, X.Y., Liu, X.X., Li, S., 2010b. Re-discussion on the metallogenic age of Zhulazhaga gold deposit in Alashan Area, Inner Mongolia: Evidence from zircon U-Pb SHRIMP age. Earth Sci. Front. 17, 178–184 in Chinese with English abstract.
Liang, P., Wu, C., Hu, X., Xie, Y.L., 2020. Textures and geochemistry of magnetite: Indications for genesis of the Late Paleozoic Laoshankou Fe-Cu-Au deposit. NW China. Ore Geol. Rev. 124, 103632.
Lin, C.N., Xie, G.A., Tian, R.S., Wang, B., Zhang, Q.L., 2022. The age and potential provenance information of Dahongshan Formation in the Langshan Mountain, the northeastern margin of the Alxa Block and its geological implications. Geol. Rev. 68, 178–184 in Chinese with English abstract.
Liu, Y.N., Fan, Y., Zhou, T.F., Xiao, X., White, N.C., Thompson, J., Hong, H.L., Zhang, L. J., 2019b. Geochemical characteristics of magnetite in Longqiao skarn iron deposit in the Middle-Lower Yangtze Metallogenic Belt, Eastern China. Miner. Depos. 54, 1229–1242.
Liu, Q., Zhao, G.C., Han, Y.G., Eizenhöfer, P.R., Zhu, Y.L., Hou, W.Z., Zhang, X.R., 2017. Timing of the final closure of the Paleo-Asian Ocean in the Alxa Terrane: Constraints from geochronology and geochemistry of Late Carboniferous to Permian gabbros and diorites. Lithos 274–275, 19–30.
Liu, Y.S., Zong, K.Q., Kelemen, P.B., Gao, S., 2008. Geochemistry and magmatic history of eclogites and ultramafic rocks from the Chinese continental scientific drill hole: Subduction and ultrahigh-pressure metamorphism of lower crustal cumulates. Chem. Geol. 247 (1–2), 133–153.
Liu, P.H., Zou, L., Tian, Z.H., Ji, L., Shi, J.R., 2019a. Determination of Late Paleozoic metamorphic event in the Langshan area, western Inner Mongolia: New evidence from LA-ICP-MS zircon U-Pb dating of the Wulashan Group. Chin. Sci. Bull. 38, 1691–1710 in Chinese with English abstract.
Ludwig, K., 2010. Isoplot/Ex version 4.1, A geochronological toolkit for Microsoft Excel. Berkeley Geochronology Center Special. Publication No. 4.
Luo, T., Deng, X.D., Li, J.W., Hu, Z.C., Zhang, W., Liu, Y.S., Zhang, J.F., 2019. U-Pb geochronology of wolframite by laser ablation inductively coupled plasma mass spectrometry. J. Anal. at. Spectrom. 34 (7), 1439–1446.
Luo, T., Zhao, H., Li, Q.L., Li, Y., Zhang, W., Guo, J.L., Liu, Y.S., Zhang, J.F., Hu, Z.C., 2020. Non-matrix-matched determination of Th-Pb ages in zircon, monazite and xenotime by laser ablation-inductively coupled plasma-mass spectrometry. Geostand. Geoanal. Res. 44 (4), 653–668.
Luo, T., Zhao, H., Zhang, W., Guo, J.L., Zong, K.Q., Liu, Y.S., Zhang, J.F., Hu, Z.C., 2021. Non-matrix-matched analysis of U-Th-Pb geochronology of bastnäsite by laser ablation inductively coupled plasma mass spectrometry. Science China (earth Sciences) 64 (4), 667–676.
McIntire, W.L., 1963. Trace element partition coefficients-a review of theory and applications to geology. Geochim. Cosmochim. Acta 27 (12), 1209–1264.
Nadoll, P., Mauk, J.L., Hayes, T.S., Koenig, A.E., Box, S.E., Box, S.E., Bookstrom, A.A., Anderson, R.G., 2012. Geochemistry of magnetite from hydrothermal ore deposits and host rocks of the Mesoproterozoic Belt Supergroup, United States. Econ. Geol. Bull. Soc. Econ. Geol. 107 (6), 1275–1292.
Nadoll, P., Angerer, T., Mauk, J.L., French, D., Walshe, J., 2014. The chemistry of hydrothermal magnetite: A review. Ore Geol. Rev. 61, 1–32.
Nadoll, P., Mauk, J.L., Leveille, R.A., Koenig, A.E., 2015. Geochemistry of magnetite from porphyry Cu and skarn deposits in the southwestern United States. Miner. Depos. 50 (4), 493–515.
Nakamura, M., Watson, E.B., 2001. Experimental study of aqueous fluid infiltration into quartzite; implications for the kinetics of fluid redistribution and grain growth driven by interfacial energy reduction. Geofluids 1 (2), 73–89.
Nielsen, R.L., Forsythe, L.M., Gallahan, W.E., Fisk, M.R., Foley, S.F., van der Laan, S.R., 1994. Major- and trace-element magnetite-melt equilibria. Chem. Geol. 117 (1–4), 167–191.
Peng, R.M., Zhai, Y.S., Wang, Z.G., Han, X.F., 2005. Discovery of double-peaking potassic volcanic rocks in Langshan Group of the Tanyaokou hydrothermal-sedimentary deposit, Inner Mongolia, and its indicating significance. Sci. China Ser. D-Earth Sci. 48 (6), 822–833.
Pi, Q.H., Liu, C.Z., Chen, Y.L., Li, Y.Q., Li, D.P., 2010. Formation epoch and genesis of intrusive rocks in Huogeqi orefield of Inner Mongolia and their relationship with copper mineralization. Miner. Depos. 29 (3), 437–451 in Chinese with English abstract.
Pi, Q.H., Zhong, R.C., Hu, R.Z., 2015. Tracing the ore-formation history of the shear-zone-controlled Huogeqi Cu-Pb-Zn deposit in Inner Mongolia, northern China, using H, O, S, and Fe isotopes. Ore Geol. Rev. 71, 263–272.
Righter, K., Leeman, W.P., Hervig, R.L., 2006. Partitioning of Ni, Co and V between spinel-structured oxides and silicate melts: Importance of spinel composition. Chem. Geol. 227 (1–2), 1–25.
Rudnick, R.L., Gao, S., 2003. Composition of the continental crust. Treatise Geochem. 3, 1–64.
Sievwright, R.H., Wilkinson, J.J., Neill, O., H.S.C., Berry, A.J., 2017. Thermodynamic controls on element partitioning between titanomagnetite and andesitic–dacitic silicate melts. Contrib. Miner. Petrol. 172 (8), 62.
Su, B.Q., 2019. Geochronology, Geochemical Characteristics and Geological Significance of Quartz-diorite from the Huogeqi Area in Inner Mongolia. Hebei Geo University, China. Master thesis (in Chinese with English abstract.
Tian, R.S., Xie, G.A., Zhu, W.B., Gao, S., 2021. Late Paleozoic magmatic flare-up in the Nuoergong-Langshan Belt, Alxa Block: Insights into tectonic evolution of the southern Paleo-Asian Ocean. Lithos 398–399, 106310.
Toplis, M.J., Corgne, A., 2002. An experimental study of element partitioning between magnetite, clinopyroxene and iron-bearing silicate liquids with particular emphasis on vanadium. Contrib. Mineral. Petrol. 144 (1), 22–37.
Wang, C., 2014. Study on the geological characteristics and ore genesis of the Oubulage copper-gold deposit in Wulatehouqi, Inner Mongolia. China University of Geoscience, China. Master thesis (in Chinese with English abstract.
Wang, Z.Z., Han, B.F., Feng, L.X., Liu, B., 2015. Geochronology, geochemistry and origins of the Paleozoic-Triassic plutons in the Langshan area, western Inner Mongolia, China. J. Asian Earth Sci. 97, 337–351.
Wang, Z.Z., Han, B.F., Feng, L.X., Liu, B., Zheng, B., Kong, L.J., 2016. Tectonic attribution of the Langshan area in western Inner Mongolia and implications for the Neoarchean-Paleoproterozoic evolution of the Western North China Craton: Evidence from LA-ICP-MS zircon U-Pb dating of the Langshan basement. Lithos 261, 278–295.
Wang, Z.Z., Han, B.F., Feng, L.X., Liu, B., Zheng, B., Kong, L.J., Qi, C.Y., 2021. Early-Middle Permian plutons in the Langshan area, western Inner Mongolia, China, and their tectonic implications. Lithos 382–383, 105934.

Wang, W.L., Teng, X.J., Liu, Y., Teng, F., Guo, S., He, P., 2017. Zircon U-Pb Chronology and Geochemical Characteristics of the Wuheertu Granite Mass in Langshan, Inner Mongolia. J. Geomech. 23 (3), 382–396 in Chinese with English abstract.
Wang, W.L., Teng, X.J., Liu, Y., Teng, F., Guo, S., He, P., Tian, J., Duan, X.L., 2018. Geochemical characteristic, LA-ICP-MS Zircon U-Pb dating and Hf isotopic composition of the haorigeshan monzogranite in the Langshan Region, Inner Mongolia. Acta Geol. Sin. 92 (11), 2227–2247 in Chinese with English abstract.
Wang, W., Teng, X., Liu, Y., Wang, R., Cheng, Y., Xin, H., Wang, S., 2020. From subduction to post-collision: Early Permian-middle Triassic magmatic records from Langshan Belt. Central Asian Orog. Belt. Geol. J. 55 (3), 2167–2184.
Wen, G., Li, J.W., Hofstra, A.H., Koenig, A.E., Lowers, H.A., Adams, D., 2017. Hydrothermal reequilibration of igneous magnetite in altered granitic plutons and its implications for magnetite classification schemes: Insights from the Handan-Xingtai iron district, North China Craton. Geochim. Cosmochim. Acta 213, 255–270.
Wu, C., Chen, H.Y., Hong, W., Li, D.F., Liang, P., Fang, J., Zhang, L.J., Lai, C., 2019. Magnetite chemistry and implications for the magmatic-hydrothermal ore-forming process: An example from the Devonian Yuleken porphyry Cu system, NW China. Chem. Geol. 522, 1–15.
Xin, H.T., Niu, S.W., Wang, H.C., Yuan, G.B., 2000. New progress in the study of the Lower Cretaceous of the Guyang area, Inner Mongolia. Re Chin. Sci. Bull. 4, 361–366 in Chinese with English abstract.
Xu, B., Charvet, J., Chen, Y., Zhao, P., Shi, G.Z., 2013. Middle Paleozoic convergent orogenic belts in western Inner Mongolia (China): framework, kinematics, geochronology and implications for tectonic evolution of the Central Asian Orogenic Belt. Gondwana Res. 23 (4), 1342–1364.
Yang, J.J., Feng, J., Li, P., 2018. Metallogenic regularity and prospecting potential of iron-copper-gold-polymetallic deposits in Alxa Area, Inner Mongolia. Geol. Resour. 27 (2), 160–165 in Chinese with English abstract.
Zhang, Y., Sun, L.X., Zhang, T.F., Teng, F., Zhang, Y., Sun, Y.W., Yang, Z.L., Xu, F., 2019. Geochronology, Geochemistry and its Tectonic Significance of the Early Paleozoic Magmatic Rocks in the Northern Langshan, Inner Mongolia. Earth Sci. 44 (1), 179–192 in Chinese with English abstract.
Zhang, Y., Sun, L.X., Zhang, T.F., Sun, Y.W., Zhang, Q., Li, Y.F., Yang, Z.L., Liu, W.G., 2020. Geochronology, Geochemistry and Sr-Nd-Hf Isotopic Composition of the Wuhua Gabbros in Langshan, Inner Mongolia: Constraints for Mantle Sources and Petrogenesis. Geosci. 34 (3), 450–465 in Chinese with English abstract.
Zhang, S.H., Zhao, Y., Song, B., Hu, J.M., Liu, S.W., Yang, Y.H., Chen, F.K., Liu, X.M., Liu, J., 2009. Contrasting Late Carboniferous and Late Permian-Middle Triassic intrusive suites from the northern margin of the North China craton: Geochronology, petrogenesis, and tectonic implications. GSA Bull. 121 (1–2), 181–200.
Zhao, W.W., Zhou, M.F., 2015. In-situ LA-ICP-MS trace elemental analyses of magnetite: The Mesozoic Tengtie skarn Fe deposit in the Nanling Range. South China. Ore Geol. Rev. 65, 872–883.
Zhao, L.J., Shao, Y.J., Zhang, Y., Li, H.B., Ahmad Shah, S., 2022. Differentiated enrichment of magnetite in the Jurassic W-Sn and Cu skarn deposits in the Nanling Range (South China) and their ore-forming processes: An example from the Huangshaping deposit. Ore Geol. Rev. 148, 105046.
Zheng, R.G., Wu, T.R., Zhang, W., Xu, C., Meng, Q.P., Zhang, Z.Y., 2014. Late Paleozoic subduction system in the northern margin of the Alxa block, Altaids: Geochronological and geochemical evidences from ophiolites. Gondwana Res. 25 (2), 842–858.
Zheng, R.G., Li, J.Y., Zhang, J., Xiao, W.J., Li, Y., 2019. Early carboniferous high Ba-Sr Alxa: Implications for Accretionary Tectonics along the Southern Central Asian Orogenic Belt. Acta Geol. Sin. (english Edition) 93 (4), 820–844.
Zheng, R.G., Li, J.Y., Zhang, J., 2021. Juvenile hafnium isotopic compositions recording a late Carboniferous-Early Triassic retreating subduction in the southern Central Asian Orogenic Belt: A case study from the southern Alxa. GSA Bull. 134 (5–6), 1375–1396.
Zhong, R.C., Li, W.B., 2016. The multistage genesis of the giant Dongshengmiao Zn-Pb-Cu deposit in western Inner Mongolia, China: Syngenetic stratabound mineralization and metamorphic remobilization. Geosci. Front. 7 (3), 529–542.
Zhong, R.C., Li, W.B., Chen, Y.J., Huo, H.L., 2012. Ore-forming conditions and genesis of the Huogeqi Cu-Pb-Zn-Fe deposit in the northern margin of the North China Craton: Evidence from ore petrologic characteristics. Ore Geol. Rev. 44, 107–120.
Zhong, R.C., Li, W.B., Chen, Y.J., Yue, D.C., Yang, Y.F., 2013. P-T-X conditions, origin, and evolution of Cu-bearing fluids of the shear zone-hosted Huogeqi Cu-(Pb-Zn-Fe) deposit, northern China. Ore Geol. Rev. 50, 83–97.
Zhong, R.C., Li, W.B., Huo, H.L., 2015. $^{39}Ar/^{40}Ar$ geochronological study on the Huogeqi Cu-Pb-Zn deposit in Inner Mongolia: A case of Proterozoic pre-enrichment followed by Indosinian metamorphogenic mineralization. Acta Petrol. Sin. 31 (6), 1735–1748 in Chinese with English abstract.